2017

Redox Stable Anode Materials for SOFC Application

Tony Thomas

Redox Stable Anode Materials for SOFC Application

Tony Thomas

Thesis submitted to the Statler College of Engineering and Mineral Resources at West Virginia University

in partial fulfillment of the requirements for the degree of

Master of Science in Materials Science and Engineering

Edward M Sabolsky, Ph.D., Chair
John Zondlo, Ph.D., Co-Chair
Xingbo Liu, Ph.D., Committee Member

Department of Mechanical and Aerospace Engineering

Morgantown, West Virginia
2017

Keywords: Redox Dilatometry, XRD, Electrical Conductivity, $CeNbO_{4+\delta}$, Nb_2TiO_7, $Sr_2MgMoO_{6-\delta}$

Abstract

Redox Stable Anode Materials for SOFC Application

Tony Thomas

The common material design for solid-oxide fuel cells (SOFCs) is based on the cermet (ceramic-metal composite) material group, for example anode compositions like nickel with yttria stabilized zirconia (Ni/YSZ). One of the main limitations of these material groups is that they may undergo unwanted thermal expansion during redox cycles, causing dimensional instability at the anode. The state-of-the-art Ni/YSZ anode experiences a linear expansion of up to 1% when oxidized, causing an irreversible microstructural change, decreasing the electrochemical activity. The problem cumulatively increases if the cell design is anode supported as this puts the electrolyte under tension, causing it to crack and leaking the fuel and oxidant gases. Currently researchers are focusing on the development of new SOFC anodes for internal reforming, lower temperature operation, and poison resistance, but there is a lack of study on the redox stability of these newly developed materials.

In this thesis work, the fundamental development of redox stable anode materials has been undertaken. Materials from perovskite, double perovskite, scheelite and double rutile structures has been considered. The material compositions include $CeNb_{1-x}W_xO_4$, $CeNb_{1-x}Mo_xO_4$, $Sr_2Mg_{1-x}Mo_{1+x}O_6$ (x = 0, 0.1, 0.2), Nb_2TiO_7 and $Nb_{1.33}Ti_{0.67}O_4$. The thermo mechanical and electrical redox stability of the various novel materials were tested by controlled-atmosphere dilatometry and four-point probe DC electrical conductivity respectively at SOFC operating temperature (800^{o}C). Based on the thermo mechanical and electrical redox results, several doping strategies were adopted in the material systems to improve their redox stability while maintaining the coefficient of Thermal Expansion (CTE) at a minimum. The qualified material system was subjected to symmetrical and fuel cell tests to analyze the polarization resistance of novel anode material as well as electrochemical activity via in situ EIS.

It was found that in $CeNbO_4$ material group, W and Mo doping seized the phase transition of $CeNbO_4$ from monoclinic to tetragonal at elevated temperature. Also the CTE of $CeNbO_4$ in air between 25 – 800^{o}C was considerably brought down from 20.77 to 13-14x10^{-6} K^{-1} by adopting this doping strategy. Regarding Nb_2TiO_7 and $Nb_{1.33}Ti_{0.67}O_4$ materials, though these materials exhibit stable phase transformation, Nb_2TiO_7 as a starting SOFC composition is not ideal due to poor electrical properties (1.35 S/cm in reducing atmosphere at 800^{o}C). Whereas, though $Nb_{1.33}Ti_{0.67}O_4$ recorded a conductivity of 85 S/cm in reducing condition, the material is mechanically not stable under redox condition at 800^{o}C. In $Sr_2Mg_{1-x}Mo_{1+x}O_6$ (x = 0, 0.1, 0.2) material system, the material with $Sr_2Mg_{0.9}Mo_{1.1}O_{6-\delta}$ composition was made both mechanically and electrical redox stable at 800^{o}C, with a CTE of 14.5x10^{-6} K^{-1} in air between 25 – 800^{o}C and electrical conduction of

0.1 S/cm in air and 17.5 S/cm in reducing atmosphere. From symmetrical cell analysis, it was analyzed that $Sr_2Mg_{0.9}Mo_{1.1}O_{6-\delta}$ had a low polarization resistance of 0.35 Ω cm^2 at 800^{o}C which make it a potential SOFC anode material.

Acknowledgement

I would like to take this opportunity to thank my supervisor Professor Edward M Sabolsky, co-supervisors Professor John Zondlo and Professor Xingbo Liu. A big thanks to Mr. Richard Hart from GE Global Research Center, our industrial partner for supporting the SOFC project. I am greatly gratified to Professor Sabolsky for extending his precious time to guide me throughout this research and giving me the opportunity to join his functional ceramic team. Thank you Professor Sabolsky, for being a great source of inspiration and motivation for this project. It was an immense pleasure working with you.

This work was completed with the funding from the US DOE project (DE-FE-0026169). I would like to extend my sincere appreciation to the DOE-NETL project manager Mr. Steven Markovich. I acknowledge the use of the WVU Shared Research Facilities to complete this work.

I would like to thank Mrs. Kathy Sabolsky, for educating me on various ceramic oxide synthesis techniques and for being the go to person for troubleshooting. I would like to express my sincere appreciation to my colleagues and friends Mr. Gunes Yakaboylu, Mr. Ozcan Ozmen, Mr. Derrick Banerjee, Ms. Alison Arnold, Mr. Kavin Sivaneri and Dr. Maria Torres for being a good sport throughout my time in the team.

Finally and most importantly I take this opportunity to extend my everlasting gratitude towards my parents Mr. P. A. Thomas and Professor Philomena Thomas for their financial support, love and care throughout my student life. I also thank my sister Mrs. Teena Job and my Brother-in-law Mr. Sudeep Job for constantly helping me and guiding me with non- academic difficulties. I love you all.

Table of Contents

List of Figures

List of Tables

Chapter 1. Literature Review on SOFC Development

1.1 Introduction to SOFC

A Solid Oxide Fuel Cell (SOFC) is an electrochemical device that converts chemical energy from a fuel (hydrogen and other forms of hydrocarbon) into useful electricity through various electrochemical reactions. Compared to a mechanical generator working on Carnot efficiency, the SOFC is more efficient as no combustion process is involved [1]. As a result, the electrical output is directly converted from the fuel enthalpy associated with the electrochemical redox process of air and fuel to form water and/or carbon dioxide [2]. Due to this fact, electrochemical fuel cells can perform at higher electrical efficiency compared to conventional electrical generators. SOFC's also take advantage of fuel flexibility unlike other electrical generators as mentioned above. The electrochemical process generates significant amount of heat that can be coupled with heat and power systems (CHP) [1]. These types of fuel cells produce very low levels of SO_x and NO_x. Figure 1, shows the operating principle of a typical SOFC system.

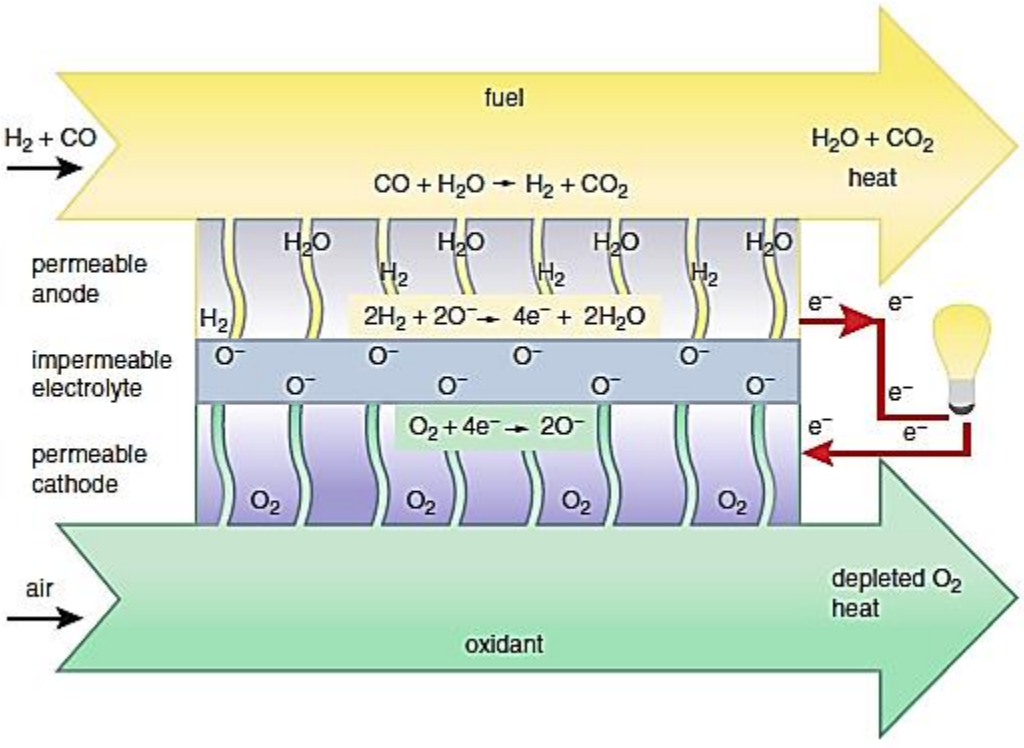

Figure 1. Operating procedure of a SOFC device [3]

As seen in Figure 1, a typical SOFC setup consists of two porous electrodes which are separated by a dense, selective, solid oxide ceramic electrolyte which conducts only oxygen ion (O^{2-}). The oxygen in the supply gas reacts with the incoming electron from the external circuit to release O^{2-} at the cathode as depicted in Figure 1. The O^{2-} migrate to the anode side through the ion conducting oxide ceramic electrolyte to react with H_2 or other forms of fuel to liberate electrons and water at the anode. The electrons generated, flow through the external circuit to the cathode side thus producing electricity. It is a constant electrochemical process, as long as the oxygen and fuel are supplied without any disruption. The next section will briefly explain the evolution of SOFC technology.

1.2 SOFC Historical Development

It all started in 1897, when Walther Nernst showed how a solid electrolyte thin rod was made electrically conductive as it was heated by an electrical appliance. The thin rod glowed upon this process and this glowing was sustained as long as the rod was resistively heated [4]. The apparatus was known as Nernst lamp. Further investigation by Nernst on materials, concluded that the pure oxide's conductivity increased by a small amount with increase in temperature, whereas the oxide mixture's electrical conductivity increased substantially at elevated temperature. This was how the state-of-the-art 85% zirconia and 15% yttria was made and was known as Nernst mass [5]. In 1943 Carl Wagner shed light on the vacancies in the anion sub-lattice of mixed oxide solid solutions and with this the conduction mechanism in Nernst lamp was explained [6]. The filament in the Nernst lamp is indeed an ion conductor and the platinum (Pt) contact acted as an air electrode. Hence the Nernst lamp can be considered the first solid electrolyte cell.

The concept of SOFC was first demonstrated by Bauer and Preis in 1937 [7]. It was Carl Wagner's pioneering work in 1943 on the conductivity of mixed oxides like doped ZrO_2, paved way for more focused study on solid electrolytes and SOFC's. Towards the end of 1960, more applications for patents and paper related to SOFC were observed in several countries [8]. In USSR, under the leadership of Karpachov various results based on cells with solid oxide electrolytes were published from the Ural branch of the Academy of Science [9]. In the US, Ruka and other scientists from Westinghouse Electric Corporation published a paper "A Solid Electrolyte Fuel Cell" in 1962 [10] which became the keystone

of Westinghouse's cathode supported tubular SOFC. They successfully tested SOFC power system ranging from 5 – 250 kW from late 1980's to early 2000s [10].

In 1962, Sandstede from the Battelle Institute in Frankfurt published the first report on the use of hydrocarbon fuel in solid oxide cell [11]. In the same time period, Kleitz from France also embarked on a fuel cell research [12]. In 1963 a patent was filed in Britain to fabricate fuel cells by depositing layers on a porous metallic substrate [13]. Takahashi from Japan, published his early results of fuel cells with solid oxide electrolytes in 1964 [14]. This early period of SOFC development saw the need to improve the electrode and interconnection materials. It was Spacil in early 1964 who found the solution to use nickel (Ni) mixed with solid electrolyte as anode to overcome the poor adhesion problem of the anode on to the solid electrolyte [15]. Oxides of uranium and indium along with different additives were proposed as cathode materials in the early 1960's until the electronically conducting perovskites dominated the world of cathodes and interconnects [16]. In 1967 the use of $La_{1-x}Sr_xCoO_3$ as the air electrode marked the beginning of the perovskite material development which was followed by $PrCoO_3$ material development. In 1969 Meadowcroft [17] proposed $La_{1-x}Sr_xCoO_3$ for the electrode, which was later used as the interconnection material in the Westinghouse SOFC program [17]. Between 1969 and 1973, there were more than 100 reported oxide materials tested as electrodes for SOFC applications [18]. A particular composition with $LaNiO_3$ doped with SrO proved to be popular in 1973 and was used in SOFC by commercial developers.

Along with the material development for SOFC, several SOFC designs were explored since mid-1980. Out of those designs, the anode supported planar SOFC stands out due to the performance and cost of manufacturing. In the present decade SOFC's are fabricated in different designs and with different cell materials for power generation from a few watts to several hundred kilowatts. The following section will briefly explain the two most popular SOFC designs used in present day applications.

1.3 SOFC Design

The cell design mainly depends on how the three active components of the cell i.e. the anode, the cathode and the electrolyte are configured based on the different cell geometries. The most popular designs are the tubular, the planar and their variants.

1.3.1 Tubular Design

The tubular SOFC's diameter can vary from as small as < 5 mm to a diameter larger than 15 mm. A typical tubular cell architecture is as shown in Figure 2.

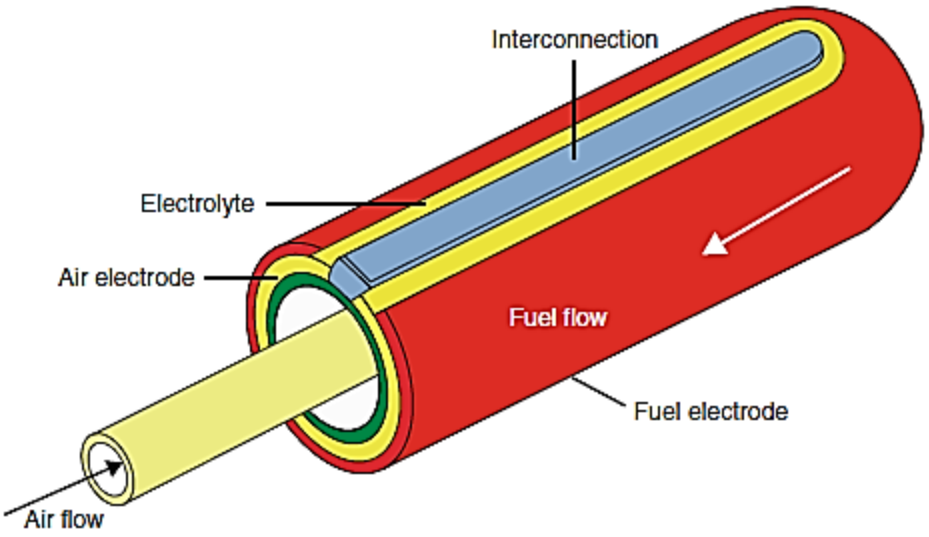

Figure 2. Schematic of Tubular SOFC design [3]

A tubular SOFC houses a porous cell tube fabricated by extruding doped lanthanum manganite and is closed at one end. The cell components, dense electrolyte, porous Ni-YSZ anode and doped lanthanum chromite interconnect are deposited either by a chemical vapor deposition process or a plasma spraying process [19]. The main advantage of the tubular design over the planar design is the absence of the high temperature seals which differentiate the oxidants from the fuel. Hence tubular designs exhibit stable performance over an extended period of time compared to planar cell design. However when it comes to power density, both the areal and volumetric power density is much lower than the planar cell and the cost of manufacturing tubular cells is higher than the planar cells.

1.3.2 Planar Design

In this type of design structure, a series of cell components is configured as flat plates and electrically connected to achieve a desirable performance. Figure 3, is the schematic representation of a typical planar SOFC cell.

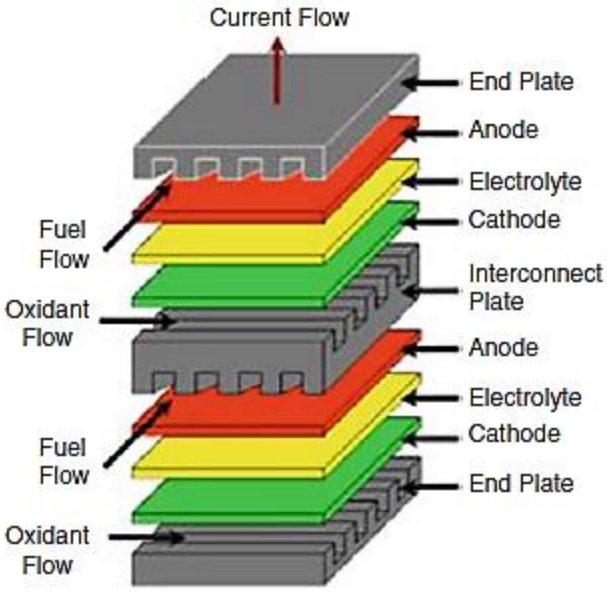

Figure 3. Schematic of a planar SOFC design [3]

The planar cell design can be electrode supported, electrolyte supported or even metal supported. Some of the advantages offered by the planar cell design over the tubular design are as follows:

a) Lower cost of manufacturing
b) Higher power density
c) Ease of manufacturing

But they require a high temperature sealant between the cell components in the SOFC stack. A stable high temperature seal development is the most challenging area in successfully commercializing a planar SOFC. The advancement in ceramic processing has enabled the fabrication of a thin electrolyte of 10 μm or thinner by tape casting or plasma spraying and as a result the anode supported stacks have been developed and tested by many SOFC developers. The next section will briefly explain the components of SOFC and the functionality they offer towards the versatility of SOFC technique.

1.4 SOFC Components

The stable operation of SOFC depends on its components, which are the solid state electrolyte, the cathode and the anode. In the coming sub-sections the functionality of the cell components along with most popular cell materials will be explained.

1.4.1 Electrolyte [20, 21]

It is the electrolyte that determines the operating temperature of a SOFC and also prevents short circuiting the electrodes. The electrolyte is responsible in maintaining the overall electrical charge balance by allowing the flow of ions. The electrolyte can be either an oxygen ion conductor or a hydrogen (proton) conductor. The difference between the ion conducting and proton conducting electrolyte is the side in which the water is produced. Though there are several oxide ceramic electrolytes at present, the most commonly used SOFC electrolyte to date is the yttria-stabilized zirconia (YSZ) with a stoichiometry of $(ZrO_2)_{0.92}(Y_2O_3)_{0.08}$. YSZ is purely an oxygen ion conductor. Here the conduction mechanism is due to ion hopping from the vacancies created by Y_2O_3. Other dopants like Mgo, Sc_2O_3, CaO are also used to stabilize ZrO_2. Some of the other noteworthy oxide ceramic electrolytes used in SOFC include:

a) Ceria doped gadolinium, GDC ($Ce_{0.9}Gd_{0.1}O_{1.95}$)
b) Ceria doped calcium ($Ce_{0.88}Ca_{0.12}O_{1.88}$)
c) Strontium cerate ($SrCe_{0.95}Yb_{0.05}O_3$
d) Barium cerate $(Bi_{0.75}Y_{0.25})_2O_3$
e) Lanthanum strontium gallium magnesium ($La_{0.8}Sr_{0.2}Ga_{0.9}Mg_{0.1}O_{2.85}$ or $La_{0.8}Sr_{0.2}Ga_{0.8}Mg_{0.2}O_3$
f) Ceria doped samarium $(Ce_{0.85}Sm_{0.15})O_{1.925}$

1.4.2 Cathode

At cathode, oxygen from air is reduced to O^{2-} ion by reacting with the electron generated at the anode as seen in the equation 1-1.

$$\frac{1}{2} O_2 (g) + 2e^{2-} \leftrightarrow O^{2-} (s) \qquad 1\text{-}1$$

Oxygen which is initially in the gas phase is reduced to oxide ion by consuming two electrons in the process. The SOFC cathode must meet the following requirements [22]

a) Chemical stability and dimensional stability during cell operation
b) High electronic conductivity to assist oxygen reduction reaction (ORR)
c) Porous to assist the transport of the oxygen molecule to the ORR sites and then transport the oxide ions to the electrode/electrolyte interface
d) Compatibility in the CTE with other cell components
e) Minimum reactivity with the electrolyte

Lanthanum strontium manganite (LSM) and lanthanum calcium manganite (LCM) offer excellent performance above 800^{o}C and also have a good CTE match with YSZ. Other cathode materials for low temperature SOFC application include:

a) Lanthanum strontium cobalite ferrite (LSCF)
b) Lanthanum strontium cobalite (LSC)
c) Lanthanum strontium ferrite (LSF)
d) Samarium strontium cobalite (SSC)
e) Praseodymium strontium manganite (PSM)

For better performance the above mentioned electrode powders are composited with electrolyte powders like YSZ, SDC and GDC. This improves the electrode performance at lower temperature as the volume of active electrochemical sites increases [23]

1.4.3 Anode

The ceramic anode is a porous solid-state membrane which allows the fuel to flow towards the electrolyte. The electrochemical oxidation of fuel takes place at the anode preferentially at certain surface sites called the triple phase boundaries (TPB's). They are the interface between the electrolyte, electrode and the gas. The oxidation of H_2 fuel occurs at the anode and can be represented as [24]:

$$H_2\,(g) + O^{2-}\,(s) \leftrightarrow H_2O\,(g) + 2e^-$$

The polarization at the anode is mainly influenced by the microstructure of the anode materials, exposed area, powder morphology and distribution of porosity for efficient fuel permeation in a high temperature, reducing atmosphere. The anode material should be highly electronically conductive with sufficient electro catalytic activity to minimize the polarization losses due to the H_2 oxidation reaction. The anode must also be chemically

and thermally stable with minimum CTE mismatch with the rest of the cell components. An ideal anode material should also be able to handle fuel flexibility with commonly used fuels like hydrogen, CO and other hydrocarbons tolerating sulfur poisoning, carbon deposition and redox stable. Metals were used initially as the fuel cell anode because of the reducing condition. Anode materials are mainly fabricated from composite electrolyte powder mixtures like YSZ and GDC. NiO/YSZ is the most commonly used anode material with the YSZ electrolyte. Its electronic conductivity ranges between 10^2 to 10^4 S/cm at 1000^{o}C. In NiO/YSZ, Ni metal provides the platform for high catalytic activity for the oxidation of hydrogen fuel. However this state-of-the-art anode material, NiO/YSZ, faces several issues like redox instability, which is due to the expansion during anodic reoxidation of Ni to NiO [25]. This expansion causes stress at the electrolyte anode interface [26, 27]. NiO-YSZ also is affected by carbon deposition and sulfur poisoning from the impurities in the fuel system [28]. Nickle is also susceptible to grain coarsening under prolonged usage at high temperature (600-1000^{o}C) [29].

Due to these issues exhibited by the state-of-the-art NiO/YSZ anode, development of novel anode materials is paramount for a stable SOFC application. The key properties that an ideal anode material should possess are mechanical redox stability and the ability to prevent poisoning of the electrode. Research and development on SOFC anode materials has led to fabrication of various types of anodes based on spinels, pyrochlores, fluorites, perovskites and layered perovskites, ceramic composites and titanate-based components. Other criteria to keep in mind while developing novel anode materials are:

a) Low polarization resistance
b) Sustainable and durable material
c) Capable of performing at intermediate temperature (600-800^{o}C)

The motivation for the current research work stems from the issues developed by the state-of-the-art NiO/YSZ and, a need for a mechanically redox stable, mixed ionic and electronically conductive anode material.

1.5 Motivation for the project

As mentioned in section 1.4.3, the state-of-the-art NiO/YSZ anode experiences a volumetric expansion of up to 1% when oxidized causing an irreversible microstructural change as seen in Figure 4.

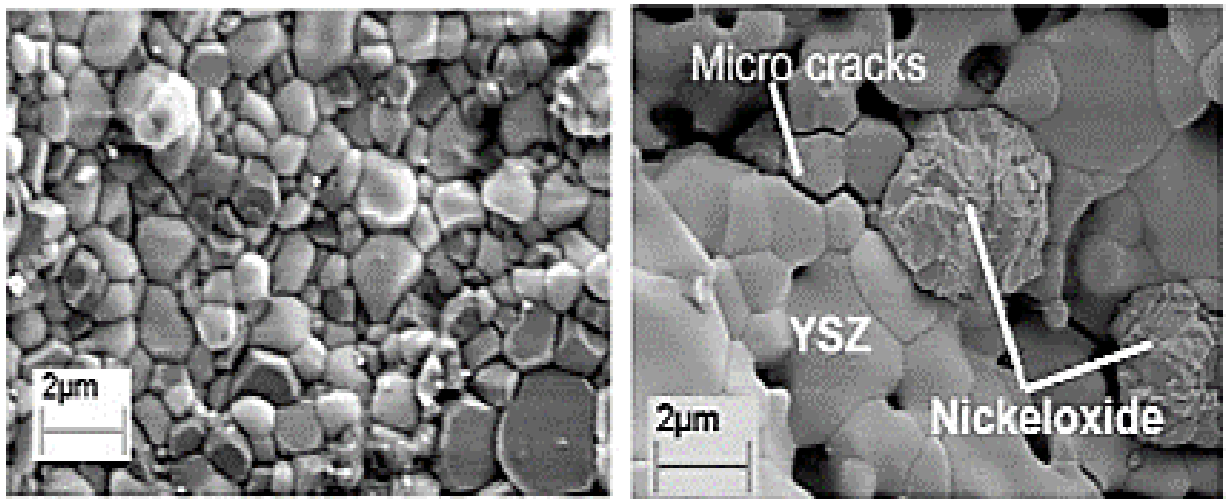

Figure 4. NiO/YSZ bulk anode. (Left) Before oxidation, (right) after 4 redox cycles [30]

The anode side of the SOFC may be subjected to an oxidizing atmosphere when there is a leak through the seal, crack in one of the stacks and also during emergency shutdown of SOFC. The expansion of the material can crack the entire cell as seen in Figure 5, resulting in the increase in anode polarization resistance as seen in Figure 6.

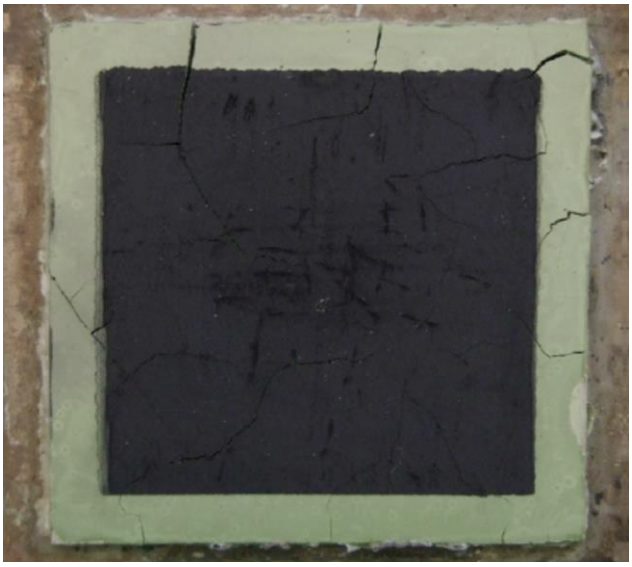

Figure 5. Anode supported cell after 1 oxidation cycle in manifold at 850ºC [31]

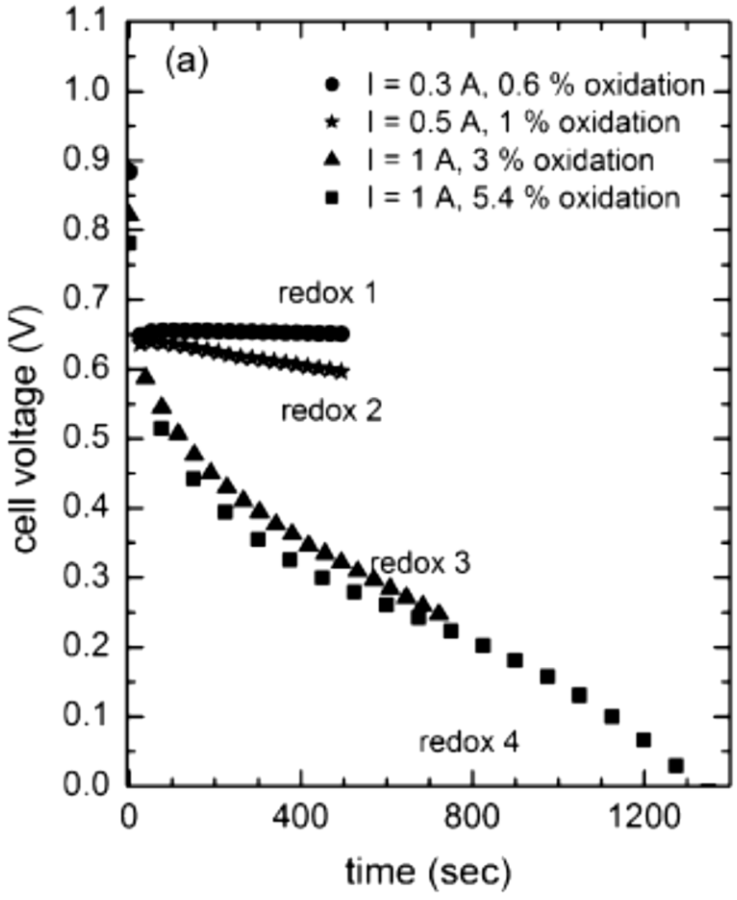

Figure 6. Cell voltage as a function of current and % oxidation at 850ºC [31]

Hence there is a need to develop highly redox-stable anode materials that can withstand a multiple number of reduction and oxidation cycles with minimum material expansion or contraction, thus leaving the cell stack unaffected and performing steadily for a long duration.

Also this project was undertaken mainly to support the GE, Global Research Center (GRC), in the development of all-ceramic metal-supported SOFC. They are adopting a non-conventional fabrication process using thermal spraying. Conventionally as seen in Figure 7a, fabrication of SOFC involves processes like tape casting, lamination, hot pressing, screen printing and sintering. It is expensive, labor intensive as well as time-consuming. As the result of this the unit price of an auxiliary SOFC unit is high. On the contrary to this, GE-GRC, is by-passing all the conventional processing routes by using thermal spraying technique. By this they can bring the unit price of SOFC system considerably down.

As seen in Figure 7b, in thermal spraying, slurry of the feedstock of the desired material is pumped through the thermal spraying gun maintained at a particular temperature (generally above 1200^{o}C). Usually the feedstock is heated by a plasma or arc and the melted material is thermally sprayed on a substrate. The advantage of thermal spraying is ease of the scalability (larger active area SOFC) of the cell without other alterations or new components.

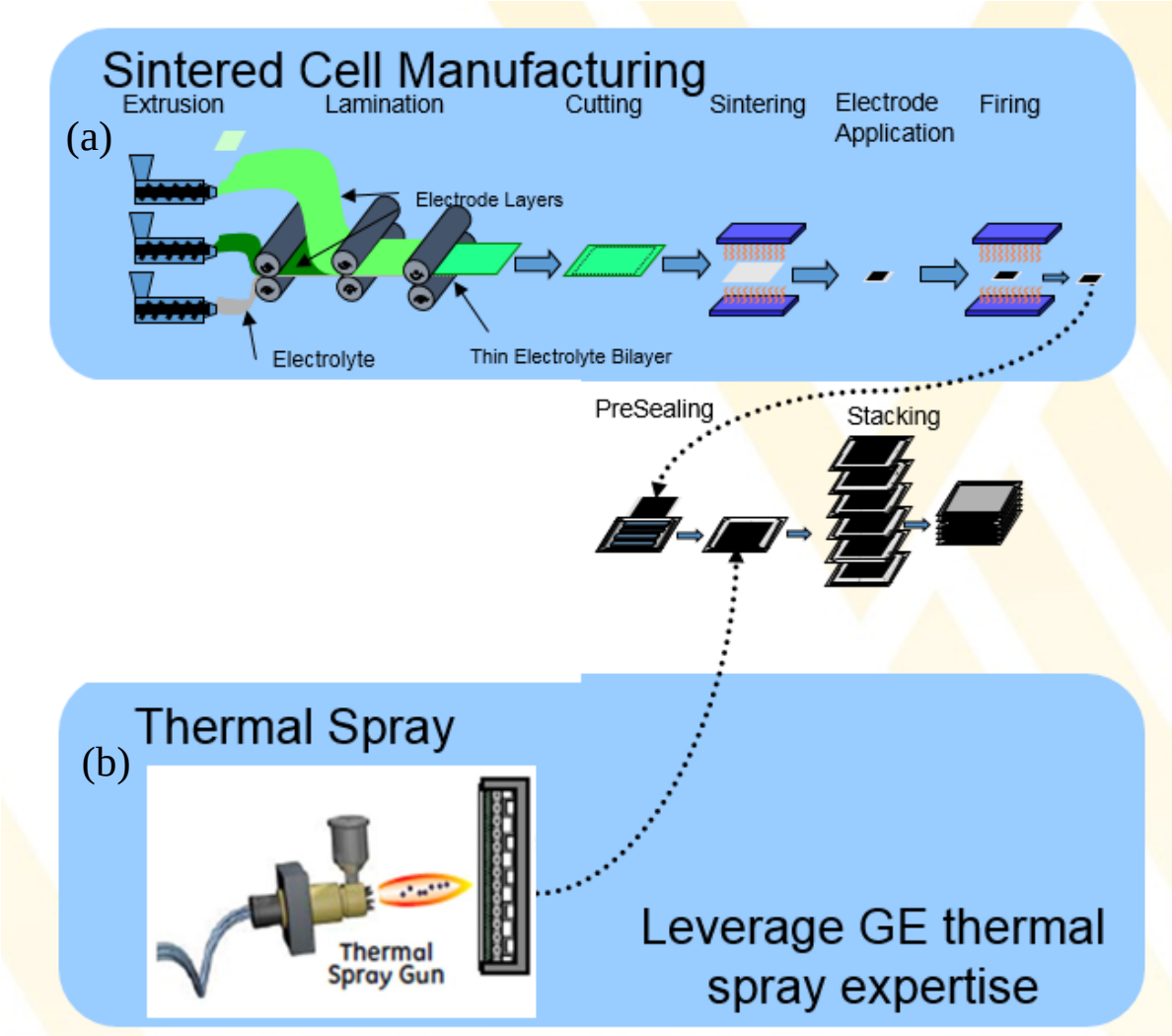

Figure 7. (a) Conventional SOFC fabrication process, (b) Thermal spraying employed by GE for fabricating all ceramic SOFC [Illustration courtesy, GE-GRC]

In this case the anode feedstock is first sprayed on to a metal substrate to a desired thickness followed by a thin dense layer of YSZ and a cathode as seen in Figure 8. Hence it is known as metal-supported SOFC as the fuel cell component is sprayed on the metal substrate layer by layer. This is a single step process as the material is sintered as soon as it passes the plasma gun (the material is heated nearly to its melting point). Hence the manufacturing cost per unit stack is considerably lower compared to a unit stack prepared by conventional SOFC fabrication techniques showed in Figure 7a. The advantage of thermal spraying over the conventional SOFC fabrication process is:

a) Integrated anode seal
b) Electrolyte is in compressed state and hence higher Triple Phase Boundary (TPB)
c) Improved anode electrical contact as it is directly sprayed on to the metal support
d) Increased active area due to higher electrical contact
e) And due to increased active area, lower anode polarization

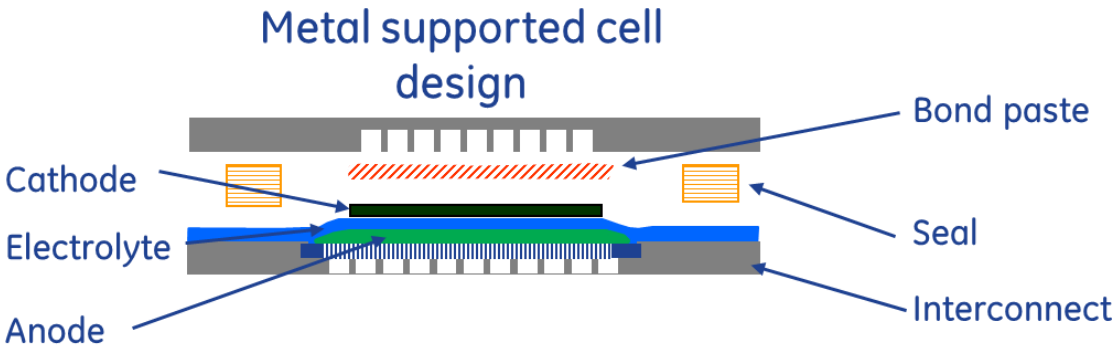

Figure 8. Metal supported SOFC architecture [Illustration Courtesy GE-GRC]

The atmosphere in the thermal spraying booth at GE is not inert and is just a normal atmosphere. Hence thermal spraying of NiO/YSZ anode is difficult due to the redox and thermal issues of the NiO/YSZ anode that were mentioned in the above section. Hence the motivation is generated to find a redox-stable anode material that can be thermally sprayed on to the metal substrate without inducing any phase instability as well as thermal instability during and after spraying process.

Several material systems from perovskites, layered perovskites, rutile and scheelite were considered in this material development study. A material screening process using high temperature redox dilatometry was developed in this study to analyze the mechanical integrity of the material under redox conditions. The next Chapter 2, explains the development of the redox testing protocol and the calibration of this testing technique using some known SOFC materials like YSZ, GDC, LST and LST/GDC.

Chapter 2. Developing High Temperature Redox Dilatometry Testing Protocol

2.1 Introduction

The porous anode is the most important component in a SOFC, as it serves as a platform to assist electrochemical reactions like the oxidation of fuel, a channel for electron transfer from the electrolyte/anode reaction sites, a pathway for fuel permeation and also for the removal of other byproducts formed at the site to maintain cell equilibrium as explained in Chapter 1. The hindrance to the performance of a SOFC is the cell degradation with time. The degradation process can occur in many forms such as coking, sulphur poisoning and coarsening of the microstructure, which interferes with the mechanical and chemical stability of the cells. An ideal anode material should have mixed ionic and electronic conductivity, chemically stable with the electrolyte, high electro-catalytic activity towards both oxidation of fuel as well as reforming of hydrocarbons for fuel flexibility, but mainly the coefficient of thermal expansion (CTE) should match the adjoining cell components. Since the anode material operates in a reducing atmosphere, high electrically conductive metal electrodes can be used in principle. Setoguchi et al. [32] did elaborate work on assessing the electrochemical activity of Co, Fe, Mn, Ni, and Ru for H_2 oxidation. From their research it was concluded that Ni has the highest electrochemical activity. Ni has a melting point of around 1450^{o}C with a CTE of 13.3 x 10^{-6} K^{-1}. Its electronic conductivity lies between 2 x 10^4 S/cm to 138 x 10^4 S/cm at 25 and 1000^{o}C respectively [33].

The state-of-the-art nickel/yttrium-stabilized zirconia (Ni/YSZ) anode material exhibits some limitation towards complete fuel flexibility, especially when using fossil fuels (with and without contaminates). This composition generally has poor tolerance towards contaminants such as phosphine and hydrogen sulfide present in the hydrocarbon fuel and may be subjected to coking [34]. Ni/YSZ also has poor redox stability and can expand irreversibly up to 2.5% by volume when oxidized [35], causing cracks in the microstructure, thus increasing cell polarization resistance. These issues led to the investigation of alternative ceramic-based anode materials excluding the Ni in the composition.

The design and development of materials is a time consuming and rigorous process. The development of state-of-the-art Ni/YSZ is a cumulative effort offered by 100's of material

scientists for nearly two decades. Designing a new material system to accommodate complex multifunctional platform like the SOFC, demands an intensive investigation paradigm. The basic material design process involves selection of the starting powder composition, a calcination study, the intrinsic and extrinsic property characterization and catalytic activity study. Only after all these studies prove positive, can one start the actual fuel cell testing. Hence development of a new anode material is time consuming, labor intensive and expensive.

In this Chapter, a preliminary screening process to speed through the anode material development is suggested. Apart from the electro-catalytic activity, the mechanical redox stability of the anode material is paramount. The present Chapter focuses on the development of a testing protocol to assess the mechanical redox behavior of the newly developed materials at SOFC operating temperatures, using a push-rod type dilatometer. Apart from the information on CTE, one can also visualize the mechanical behavior of the material in both oxidizing and reducing atmospheres. From this study it is also possible to measure the percentage of volumetric change experienced by the material upon redox cycling and mainly obtain the information on the time and number of redox cycles the material can withstand before failure. This type of material information is valuable from a commercial point of view; in that it provides warranty on the fuel cell stacks and aids in the development of guide lines for the safe operation of the product. In this study, the high-temperature testing protocol is developed and calibrated using well-known materials like YSZ, lanthanum strontium titanate and GDC. The data obtained from the study are compared with that in the literature to obtain confidence in the measurement system, so that the methodology can be implemented on novel anode materials.

2.2 Experimental

Powder samples of the $La_{0.35}Sr_{0.65}TiO_3$ (LST) were prepared via a solid-state synthesis route using $SrCO_3$ (Alfa Aesar, 97.5%), La_2O_3 (Alfa Aesar, 99.5% min) and TiO_2 (Alfa Aesar, 99.5%). All the above chemical compounds were stoichiometrically mixed in an attrition mill for 4 h using zirconia milling media in ethanol. The milled powder was calcined in air at 1500^oC for 4 h. The YSZ sample was prepared using 8YSZ (8 mol% doped yttria, Daiichi Kigenso Kagaku Kogoyo Co., Ltd.) powder while the GDC (GDC20-M, Fuelcellmaterials.com) samples were prepared using $Gd_{0.2}Ce_{0.8}O_2$ powder with 3.2

m^2/g surface area. For dilatometry testing, ~8.5 grams of the above mentioned powder were uniaxially pressed at room temperature into a cylindrical pellet of 30 mm diameter and 2.5 mm thickness and all the test samples were sintered in air. The thermomechanical redox stability of the material was studied using the NETSZCH DIL 402C dilatometer. Compressed air was used to simulate oxidizing atmosphere and forming gas (5%H_2, 95%N_2) was used to simulate reducing atmosphere during the dilatometry test.

2.3 Results and discussion

2.3.1 Development of testing protocol

LST, YSZ, GDC and LST/GDC (50/50 vol%) composite were chosen for the development of the testing protocol as these compositions are extensively studied and the redox data is readily available in the literature [36-37] LST was sintered in air at 1500^{o}C for 4 h to obtain a porosity of 35%. GDC was sintered in air at 1300^{o}C for 4 h to obtain a porosity of 33%. YSZ was sintered in air at 1450^{o}C for 4 h to obtain a porosity of 4%, and the LST/GDC composite was sintered in air at 1500^{o}C for 4 h to obtain a porosity of 33%. A bar sample of 25L x 2.5W x 2.5t mm as shown in Figure 9, was cut from the sintered cylindrical pellets and subjected to dilatometry testing.

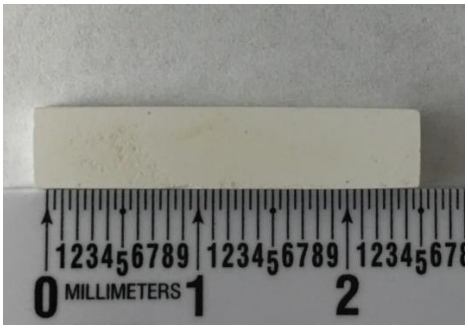

Figure 9. LST sample prepared for redox dilatometry test

To test the thermal redox stability, all the above mentioned samples were subjected to redox dilatometry between 25 – 800^{o}C as per the protocol shown in Figure 10. Segment 1-2 is the ramping stage to 800^{o}C at 3^{o}C/min in air. Segment 2-3 is the isothermal hold for 2 h at 800^{o}C before the redox cycling for thermal stabilization. Segment 3-7 is an isothermal hold for 20 h at 800^{o}C with automated atmospheric change from oxidizing (compressed air) to reducing (forming gas, 5%H_2-95%N_2), with each cycle performed for 10 h. Segment 7-8 is ramping down the temperature to room temperature at 3^{o}C/min in air. The present

optimized testing protocol is more apt for testing the thermal redox stability of novel SOFC anode materials developed.

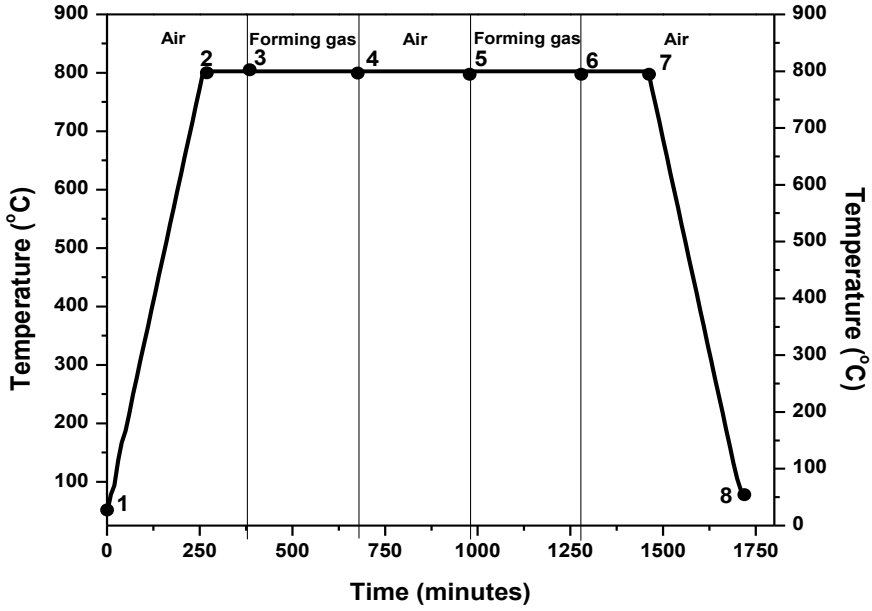

Figure 10. Redox dilatometry testing protocol

2.3.2 Calibration of test protocol with known materials

Figure 11 is the thermal redox data of 8YSZ between 25-800ºC. 8YSZ is the most commonly used electrolyte in the SOFC. The sample has a CTE of 10.83×10^{-6} K^{-1} in air between 25-800ºC. The data are comparable to Yasuda et al. [38] who reported the CTE of 10.5×10^{-6} K^{-1} at 800ºC. The redox behavior of 8YSZ has not been reported before elsewhere in this particular modus. 8YSZ is thermally redox stable for up to two redox cycles with a minimal of 0.004% volumetric reduction in the first reducing cycle followed by 0.005% volumetric reduction in the second reducing cycle. Nevertheless, the minimal volumetric reduction is reversible in nature. The difference in the percentage change from the two cycles (0.001%) can be accounted for permanent microscopic deformation due to lattice reduction and expansion upon redox cycling.

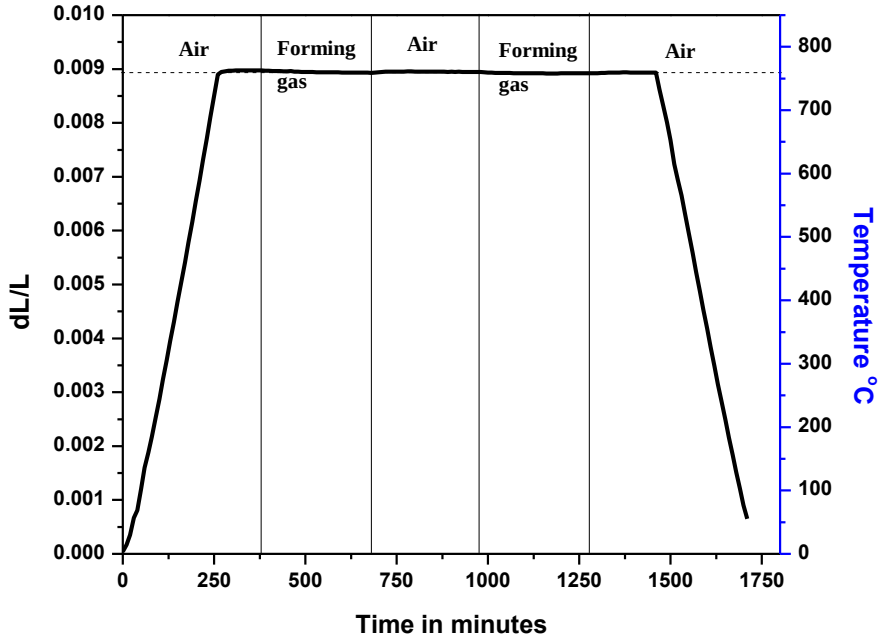

Figure 11. Thermal Redox dilatometry of 8YSZ at 800ºC

GDC was chosen for the calibration studies, as Mogensen [39] did a similar type of thermal redox study and the data obtained can be matched with real experimental results from his work. Gd doped CeO_2 is a common SOFC electrolyte barrier layer and a catalyst. It is known to reduce easily to form a mixed conducting material. Figure 12 shows the thermal redox behavior of GDC at 800ºC. Like CeO_2 the doped CeO_2 experiences a volumetric expansion of up to 0.18% in a reducing atmosphere and it is reversible in nature as seen in the second redox cycle. The material expands by same amount in the second cycle, confirming absence of any permanent deformation during the lattice expansion from the first cycle. The volumetric expansion of GDC was also observed in Mogensen's work. The volumetric expansion is due to the formation of a lower valent oxide during the reduction phase, thus expanding the CeO_2 flourite lattice [39]. From this testing protocol, the CTE was found to be 13.23×10^{-6} K^{-1} between 25-800ºC in air and this data is comparable to Hayashi et al. [37] work.

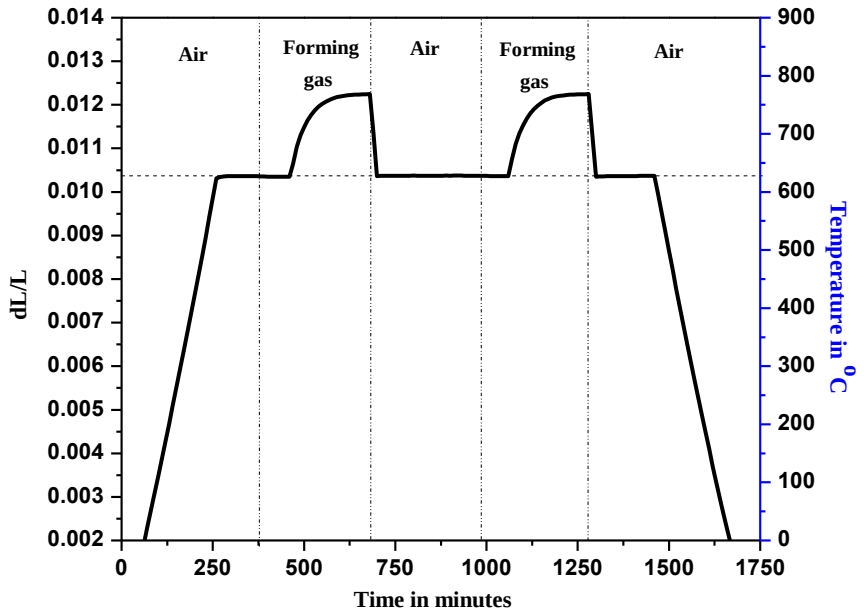

Figure 12. Thermal redox dilatometry of GDC at 800ºC

To attain thorough confidence in the measurement system, further testing was carried out with $La_{0.35}Sr_{0.65}TiO_3$ (LST). Lanthanum Strontium Titanate (LST) is one of the most extensively studied perovskite anode compositions due to its thermal stability in a redox atmosphere. Strontium titanate exhibits n-type semi-conducting upon donor doping (La^{3+}) and its electrical conductivity increases with the donor doping in a reducing atmosphere. Lanthanum is a stable trivalent element and hence, LST exhibits high thermal stability over Ni/YSZ. Figure 13 is the thermal redox data of LST at 800ºC. Unlike GDC (Figure 12), the material experiences a volumetric reduction as low as 0.01% in the reducing atmosphere and in the consecutive cycles it shows similar reducing behavior, thus exhibiting reversible redox ability. It has a CTE of around 12.51×10^{-6} K^{-1}, which is lower than Ni/YSZ. The quantifiable redox data of LST published in this work is first of its kind and can help the SOFC research community in better anode material selection using such data.

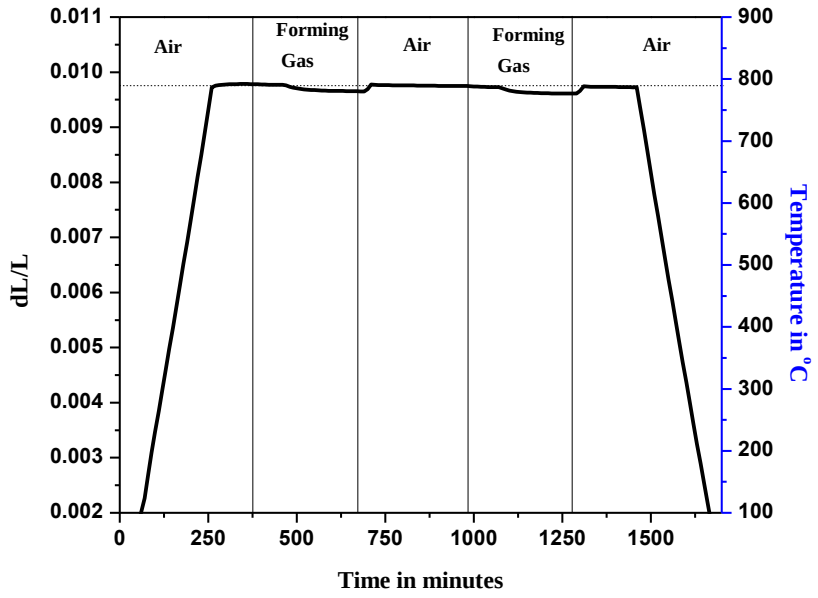

Figure 13. Thermal redox data of LST at 800°C

This type of measurement can also be used to study the thermal redox behaviour of composite materials. The data obtained can help to understand which material property is dominant in the composite. For example, Figure 14 shows the thermal redox data of the LST/GDC (50/50 vol%) composite. Here the composite exhibits a similar thermal expansion property of GDC as seen in Figure 12. There is a volumetric expansion of 0.14% in the first reducing cycle and 0.13% in the second reducing cycle. An interesting fact is that the amount of volumetric expansion of GDC decreases when composited with LST by 0.04%. There is also an increase in CTE when composited. GDC has a CTE of 13.23×10^{-6} K^{-1} between 25-800°C in air and the LST/GDC has a CTE of 13.33×10^{-6} K^{-1} between 25-800°C in air. The slight increase in CTE can be attributed to the formation of a secondary phase, which needs to be confirmed. Nonetheless the study shows how such tests and data can be interpreted and is valuable in the world of material science.

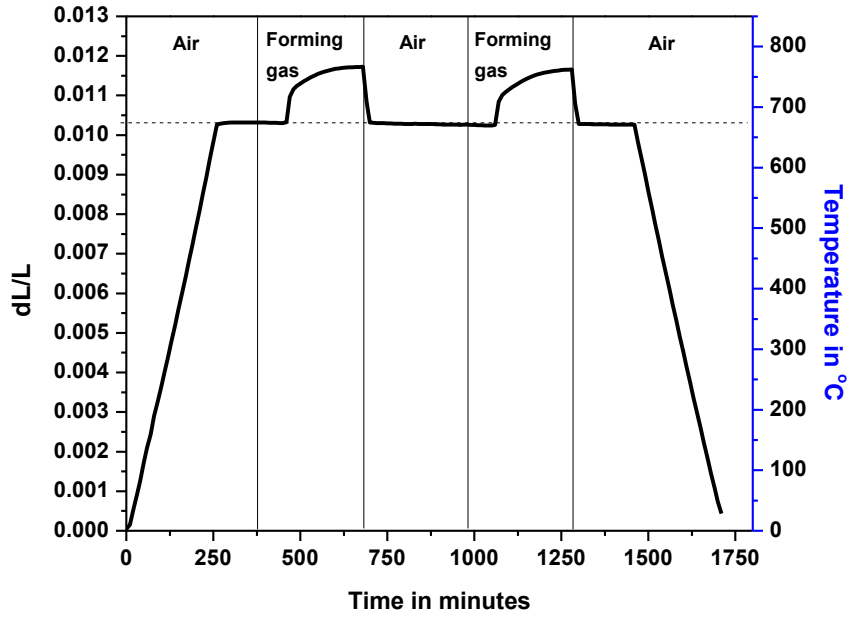

Figure 14. Thermal redox data of LST at 800°C

2.4 Conclusion

The need for a thermally redox stable anode material in SOFC is a necessity from the commercial point of view. But the material development process is lethargic, labor intensive and expensive. This calls for a preliminary screening process to assess the paramount features of an SOFC anode, mainly the CTE and its thermal redox behavior. This work illustrates the redox dilatometry technique to identify the redox behavior of any novel anode material. From the data obtained from such a technique it is possible to identify how a material lattice responds in a reducing atmosphere. The extent of the volumetric strains the material lattice experiences can be quantified from this type of measurement technique. Here the testing protocol to analyze the redox behavior of SOFC materials has been established and calibrated using known materials like GDC, 8YSZ, LST and LST/GDC (50/50 vol%). The data obtained from the calibration studies matches with the ones in the literature, providing more confidence in this thermal redox testing protocol. This testing methodology provides a platform to screen the newly developed anode materials before further characterizations are carried out.

Chapter 3. Effect of W and Mo Doping on the Redox Properties of $CeNbO_{4+\delta}$

3.1 Introduction

Currently SOFC's operate on well-established oxide ceramic materials like LSM (Lanthanum Strontium Manganite) and LSCF (Lanthanum Strontium Cobalt Ferrite) as the cathode, YSZ (Yttria Stabilized Zirconia) as the electrolyte and state-of-the-art Nickle oxide/ Yttria Stabilized Zirconia (Ni/YSZ) [40-42] as the anode. Though scientists have been able to improve the operating efficiency (from 30 to 60%) [3] and performance of the SOFC compared to the past, these cathode and anode materials exhibit significant instability when subjected to long term practical application in the temperature range 400 – 600^{o}C. Hence to make SOFC's commercially feasible, a substantial effort is required to increase their long term stability and reduce the unit cost. For this purpose current research is centered on anode and cathode compositions for maximum stability and electrochemical activity with focused emphasis on electrode microstructure engineering.

The above mentioned instability problems can be partially solved by reducing the SOFC operating temperature down to 400 – 600^{o}C with optimized oxide ceramics that can deliver high power density and sufficient durability in this intermediate-temperature (IT) range. Ironically, lowering the operating temperature reflects poorly on the overall performance of the cell, as the activation energies for the electrochemical activities usually are higher than those for oxygen ion transport in the solid electrolyte [43-45]. Hence novel cathode and anode compositions are sought with high electrochemical activity and high oxygen ion conductivity in the IT range, in order to suppress degradation due to high operating temperatures as well as thermal cycling.

Keeping these objectives in mind, researchers developed hyper-stoichiometric materials with high ionic conductivity and associated low activation energy in the IT range. This led to materials with various structural types which include Ruddlesden-Popper series materials like K_2NiF_4 type oxides, derivatives of perovskite, fluorite and pyrochlores. The present research focuses on $CeNbO_{4+\delta}$, a scheelite material with a monoclinic fergusonite structure (I2/a) at room temperature and a possible transition to tetragonal scheelite polymorphs at elevated temperature approximately above 700^{o}C [46]. Cerium niobate

exhibits a wide range of oxygen stoichiometries and can form four unique compositions identified as $CeNbO_4$, $CeNbO_{4.08}$, $CeNbO_{4.25}$ and $CeNbO_{4.33}$ [47]. The primary investigation on $CeTaO_{4+\delta}$ shed light into the interstitial oxygen sites present in these material groups and elucidated their high oxide ion conductivity [48]. In cerium niobate, the excess oxygen is accommodated in the interstitial sites during the shift in cerium oxidation state from Ce^{3+} to Ce^{4+}. It also exhibits mixed ionic-electronic conduction at higher temperature [49]. Hence they can be apt materials for the anode in SOFC due to its mixed conduction properties. However cerium niobate exhibits isothermal expansion during the shift in the cerium oxidation state upon redox cycling [47-49], which causes cell cracking, as it expands or contracts relative to the other supporting layers.

Therefore an effort has been made to make the cerium niobate more phase stable and improve its mixed conduction properties at elevated temperature by doping the B-site niobium with tungsten ($CeNb_{1-x}W_xO_{4+\delta}$) and molybdenum ($CeNb_{1-x}Mo_xO_{4+\delta}$) where x = 0.1 and 0.2. In this Chapter we report the effect of W and Mo doping on the thermal and electrical properties of cerium niobate in redox conditions. The change in the oxidation states of Ce, Nb, Mo and W was studied along with the thermal behavior of these novel compositions in a controlled atmosphere to assess the stability of these novel compositions are suitable as anode material in SOFC.

3.2 Experimental

3.2.2 Powder preparation

Powder samples of the $CeNb_{1-x}W_xO_{4+\delta}$, $CeNb_{1-x}Mo_xO_{4+\delta}$ and $CeNbO_{4+\delta}$, where x = 0.1 and 0.2 were prepared via a generic solid-state synthesis route using Nb_2O_5 (Aldrich, 99.9%), MO_3 (Alfa Aesar, 99.5% min), WO_3 (Alfa Aesar, 99.8%) and CeO_2. CeO_2 was co-precipitated from cerium ammonium nitrate in a base solution at constant pH 10, controlled by adding ammonium hydroxide. The gel was washed at ambient temperature and pressure with isopropyl alcohol to remove all the ammonium nitrate. The gel was dried at room temperature and calcined at 800^{o}C for 4 hours in air. All the above chemical compounds were stoichiometrically mixed in an attrition mill for 4 hours using zirconia milling media in ethanol for 4 hours. The milled mixture was dried at 80^{o}C for 24 hours and calcined at

1500^{o}C for 4 hours in air. Here δ is the excess oxygen in material structure, which makes the material hyper stoichiometric.

3.2.3 Phase analysis

Phase purity of the powder sample was analyzed using PANalytical X'Pert Pro X-ray diffractometer with Cu-$K_{\alpha 1}$ of 1.5406 Å wavelength. Oxidation states of the elements in the synthesized compounds were analyzed using X-ray induced Photoelectron Spectroscopy (XPS) operated at 15 kV and 25W using Al Kα (1486.6 eV) radiation. The powder particles were analyzed by a combination of 117.40 eV survey scans and 23.50 eV detailed scans of peaks of interest. A 0.5 eV step was used for each survey scan and a 0.05 eV step for the narrow scans over an area of 100 μm^2. All binding energies of C, O, Mo, W, Nb and Ce were referenced to C 1s at 284.5 eV.

3.2.4 Thermomechanical analysis

The amount of oxygen uptake was determined from thermogravimetric analysis (TGA) using a PerkinElmer Pyris 1 analyzer. Approximately 25 mg of powder sample was subjected to Temperature Programmed Oxidation (TPO) and Temperature Programmed Reduction (TPR) analysis in air and argon respectively up to 1000^{o}C at a heating rate of 10^{o}C/min. The thermomechanical redox stability of the material was studied using the NETSZCH DIL 402C dilatometer. 8.5 grams of powder samples were uniaxially pressed at 1 ton of force per unit area and sintered at 1500^{o}C in air for 2 hours to prepare bulk bar samples of 25 mm in length and 2.5mm in width and thickness for this study. Compressed air was used for the oxidizing atmosphere and forming gas (5% H_2 - 95%N_2) was used for the reducing atmosphere. A sapphire standard was used to calibrate the dilatometer before the actual tests.

3.2.5 Electrical analysis

Bulk bar samples of 25 mm in length and 2.5mm in width and thickness as shown in Figure 9, were used for a four-4 point DC total electrical conductivity measurement with a constant current of 20 mA. Four notches were cut on the bar samples and platinum wire was wound in the notch secured by platinum paste. All the measurements were taken between 25 – 800^{o}C temperature range using Keithley 2100 digital multimeter in both

oxidizing (compressed air) and reducing atmosphere (forming gas: 5%H_2-95%N_2). YSZ standard was used to calibrate the test rig, before all the test sample measurements.

3.3 Results

3.3.1 XRD Analysis

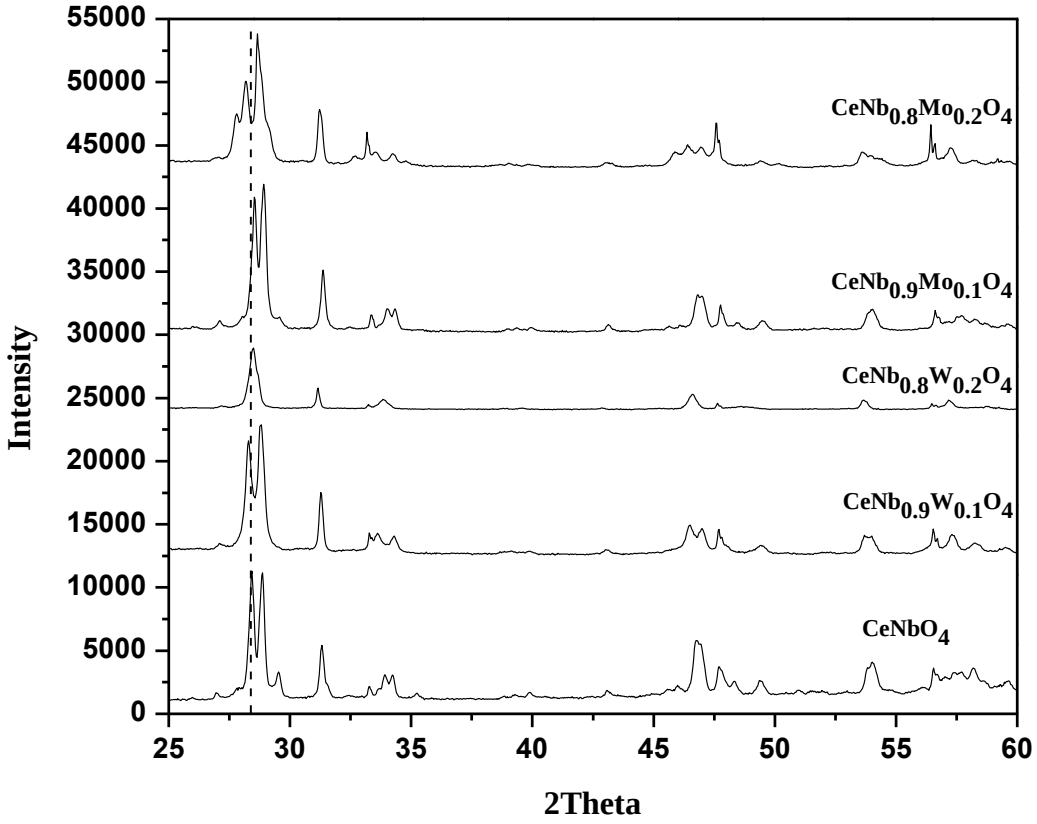

Figure 15. XRD analysis of $CeNb_{1-x}W_xO_{4+\delta}$, $CeNb_{1-x}Mo_xO_{4+\delta}$ and $CeNbO_4$ where x = 0.1 and 0.2. Materials were calcined at 1500°C for 4 hours in air

Figure 15 shows the XRD pattern of the $CeNb_{1-x}W_xO_{4+\delta}$, $CeNb_{1-x}Mo_xO_{4+\delta}$ and $CeNbO_{4+\delta}$, where x = 0.1 and 0.2 performed at room temperature in air. The XRD pattern of the primary un-doped $CeNbO_{4+\delta}$ is more inclined towards the Monoclinic I2/a crystal system with the remaining peaks matching a Tetragonal I41/a crystal system. This combination of crystal systems can be observed in $CeNb_{0.9}W_{0.1}O_{4+\delta}$ and $CeNb_{0.9}Mo_{0.1}O_{4+\delta}$ except for $CeNb_{0.8}W_{0.2}O_{4+\delta}$ which is an unary phase Tetragonal I41/a as seen in Figure 15. The occurrence of the biphasic crystal system in this material group has also been reported by

Skinner et al. [50]. In $CeNb_{0.8}Mo_{0.2}O_{4+\delta}$ system primary phase is Monoclinic I2/a, with the secondary inclusion of Ce_2MoO_6 which is cubic in nature. Hence, this material system has been excluded from further experimentation. As the dominant phase in the material systems under review is Monoclinic I2/a, the deviation from the 100% peak of Monoclinic I2/a (vertical dashed line in Figure 15) in the reviewed material system is shown in Table 1 as the function of lattice strain calculated using the Scherrer equation.

Table 1. The change in lattice strain in $CeNbO_{4+\delta}$ upon doping

Material System	Lattice Strain
$CeNbO_{4+\delta}$	0.0028
$CeNb_{0.9}W_{0.1}O_{4+\delta}$	0.0039
$CeNb_{0.8}W_{0.2}O_{4+\delta}$	0.0039
$CeNb_{0.9}Mo_{0.1}O_{4+\delta}$	0.0033

From Table 1, it is evident that the lattice strain increases with doping as a result of expansion in the unit cell. Also from the Figure 15, it can be observed that the 100% peak of the B-site doped compositions shifts gradually towards the left (vertical dashed line as the reference of original position) upon doping $CeNbO_{4+\delta}$, which is an obvious consequence of an increase in unit cell parameters.

3.3.2 XPS

XPS analysis was carried out for the as-synthesized $CeNbO_4$, $CeNb_{0.9}Mo_{0.1}O_4$ and $CeNb_{0.8}W_{0.2}O_4$ powder samples. $CeNb_{0.9}W_{0.1}O_4$ was excluded due to the similar spectral output. Here oxygen adsorption has been investigated in detail. If oxygen is chemisorbed into anion vacancies, it will be considered as a lattice ion since it is physically and thermodynamically indistinguishable from its lattice oxygen ion counterparts. Another possible form is interstitial oxygen ion where oxygen is adsorbed into tetrahedral and octahedral interstitial sites.

Figure 16 shows the O 1s, Nb 3p and Ce 3d photoelectron lines for $CeNbO_4$, $CeNb_{0.9}Mo_{0.1}O_4$ and $CeNb_{0.8}W_{0.2}O_4$. To fit the high resolution spectra, Gaussian–Lorentzian line shapes were used along with Shirley background subtraction for accurate

peak area determination for all peak analysis conducted in this work. On transition metal oxides, it is widely accepted that there are two temperature maxima for the adsorption of oxygen, they are 25°C and just above 300°C. However this value is higher for the interstitially adsorbed O^{2-} ions [51]. After deconvolution of the O 1s spectrum, three main chemical states of the oxygen were determined for $CeNbO_4$, $CeNb_{0.9}Mo_{0.1}O_4$ and $CeNb_{0.8}W_{0.2}O_4$. Table 2 show the details for the binding energy and FWHM values in addition to atomic concentration (at %) for all the elements investigated in this work.

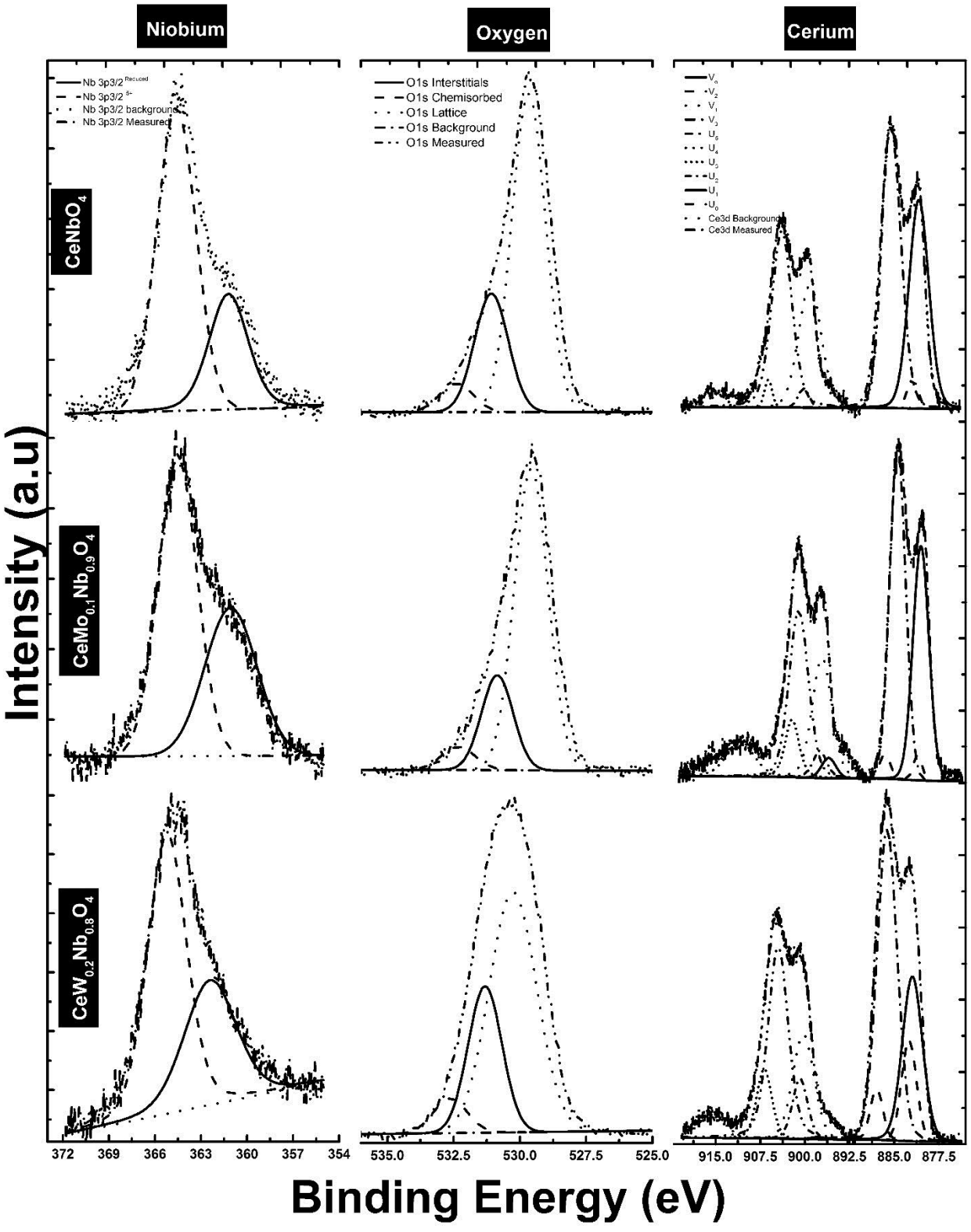

Figure 16. 3p, 1s and 3d photoelectron lines for Nb, O and Ce, respectively

Table 2. Chemical state quantification

	$CeNb_{0.9}Mo_{0.1}O_4$			$CeNb_{0.8}W_{0.2}O_4$			$CeNbO_4$		
	FWHM	**B.E (eV)**	**at%**	**FWHM (a.u)**	**B.E (eV)**	**at%**	**FWHM**	**B.E (eV)**	**at%**
Ce^{3+} $3d_{5/2}$	3.5	881.3	82	4	881.9	76	3.92	880.9	97.3
Ce^{4+} $3d_{5/2}$	1.92	881.9	18	2.97	882.5	24	2.2	881.9	6.7
$Nb^{Reduced}$	4	361.06	40	4	362.41	37	3	361.21	20
Nb^{5+}	4	364.52	60	4	365.22	63	3	364.64	80
$W^{4+}4d_{5/2}$	-	-	-	3.53	242.33	32	-	-	-
$W^{5+}4d_{5/2}$	-	-	-	3.77	244.74	31	-	-	-
$W^{6+}4d_{5/2}$	-	-	-	3.27	248.01	37	-	-	-
$O_{interstitials}$	1.4	530.85	19.6	1.5	531.31	23.4	1.5	531.07	22
$O_{lattice}$	1.5/1.5	529.58 /528.6	75.2	2.11/1.5	530.26/529.51	71	1.5/1.4	529.67/528.75	73
O^{2-} Chemisorbe	1.5	532.33	5.2	1.5	532.63	5.6	1.5	532.40	5

Chemisorbed O^{2-} ion was measured and showed a good match with the binding energies found in the literature [51-58]. Interstitial O^{2-} ions were also detected at very close proximity in all the three compounds. However the lattice oxygen binding energy (0.6 eV) was higher in $CeNb_{0.8}W_{0.2}O_4$, and this is mainly due to successful substitution of W into the Nb-site and the local effects of the W^{6+} oxidation state. But for Ce^{3+} and Ce^{4+}

quantification [59, 60], the chemisorbed O^{2-} route is not possible due to the broad feature of the O^{2-} peak, since the metals have multiple oxidation states. Hence it has been always challenging to characterize cerium containing compounds as they exhibit complicated hybridization between Ce 4f and O 2p states and satellite rich features. There exist 10 peaks in the 3d main photoelectron line of Ce [60-64].

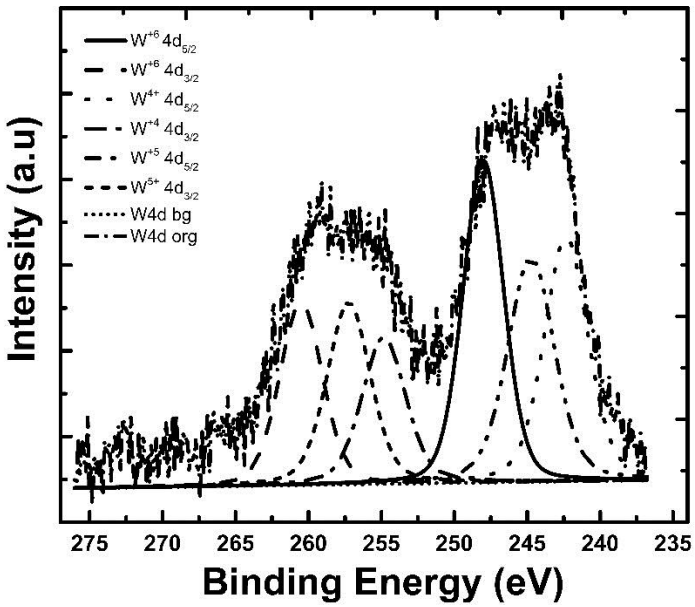

Figure 17. 4d photoelectron line of W in $CeNb_{0.8}W_{0.2}O_4$

In the Figure 16, V_0, V_1, V_2, and V_3 peaks are attributed to Ce^{3+}, while U_0, U_1, U_2, U_3, U_4, and U_5 are the typical peaks of Ce^{4+} ions. The XPS investigation indicates that the Ce^{3+} and Ce^{4+} species can be differentiated with distinct line shapes corresponding to various final states. The satellite peak U_5 is a characteristic fingerprint of tetravalent Ce^{4+}. This satellite does not exist in the spectrum of the Ce^{3+} oxidation state. As seen in Figure16, there are three distinct envelopes containing all ten peaks attributed to Ce^{3+} and Ce^{4+} oxidation states positioned approximately around 880-890 eV, 895-910 eV, and 915 eV (Refer to Table 3). A~ 1.0 eV increase in the V_0 and U_0 for W substituted sample was observed in comparison to the un-doped and the Mo substituted sample. Ce^{3+} oxide is characterized by two pairs of spin–orbit split doublets with two peaks, V_1 and V_3 positioned around 885 and 903 eV, respectively. The other doublet (V_0 and V_2) arises at around 881 and 899 eV, respectively.

Table 3. XPS binding energies of de-convoluted peaks of the Ce (3d) spectrum

	Ce^{3+}				Ce^{4+}					
Composition	V_0	V_1	V_2	V_3	U_o	U_1	U_2	U_3	U_4	U_5
$CeNbO_4$	880.9	885.6	889.3	903.9	881.9	887.9	898.2	900.2	906.2	915.6
$CeMo_{0.1}Nb_{0.9}O_4$	881.3	885.6	899.6	903.9	881.9	887.9	898.4	900.0	905.2	914.8
$CeW_{0.2}Nb_{0.8}O_4$	881.9	886.2	900.3	904.5	882.5	887.9	897.8	900.8	906.8	915.6

The intensity of this component does not directly represent the corresponding amount of Ce^{4+} [59]. A semi-quantitative analysis of the integrated peak area can be completed by following the formula presented in equation 3-1 [61]. Based on this calculation the concentrations of Ce^{3+} and Ce^{4+} ions in the samples were evaluated. $CeNbO_4$ contains 6.7 at% of Ce^{4+}, while W substituted sample had 24 at% of Ce^{4+}. This is mainly due to multiple valence states exhibited by W. The Mo substitution was not successful due to the high vapor pressure of Mo and the small amount of the Mo phase. The substitution attempt led to an increase in the reduced chemical state of the Nb in addition to the decrease in its amount and this was compensated by the increase in the Ce^{4+} up to 18 at%.

$$[Ce^{3+}] = \frac{[Ce^{3+}]}{[Ce^{3+}]+[Ce^{4+}]} = \frac{I_{V_0}+I_{V_1}+I_{V_2}+I_{V_3}}{I_{V_0}+I_{V_1}+I_{V_2}+I_{V_3}+I_{U_0}+I_{U_1}+I_{U_2}+I_{U_3}+I_{U_4}+I_{U_5}} \quad (3\text{-}1)$$

Niobium mainly appears in three different stable oxidation states i.e. 2^+, 4^+ and 5^+. The major photoelectron line of Nb is 3d, however due to the complex nature of compositions used in this work, the $3p_{3/2}$ line was chosen to be investigated as it does not have an interference from the other constituent elemental photoelectron lines. The available literature for Nb $3p_{3/2}$ lines report that for Nb^0, $3p_{3/2}$ varies from 360.10 to 360.50 eV, for Nb^{+5} the same line varies from 365.6 to 366.5 eV [65-67]. Therefore it can be interpreted that Nb has two chemical states, Nb^{5+} and $Nb^{reduced}$, as the latter consists of 2^+, 3^+ and 4^+ oxidation states. This claim is based on two phenomena that occur simultaneously, the

large FWHM value and the lower binding energy for $3p_{3/2}$ photoelectron lines for Nb. The amount of each oxidation state is given in Table 2. The core level spectra containing W 4d are shown in Figure 16. The W 4d photoelectron line was examined due to the fact that 4f line is in a strong match with the other constituent elemental lines. The W $4d_{5/2}$ and $4d_{3/2}$ peaks are well-resolved and the fitting process was completed with a high degree of confidence. The W $4d_{5/2}$ peak position at 248.0 eV, is attributed to an oxidation state of 6^+. Further analysis with the spectra for W 4d revealed good fits of the 4^+ and 5^+ oxidation states, confirming that the tungsten resides in a mixed valence state including 4^+, 5^+ and 6^+ with 37, 31 and 32 at %, respectively in the tested samples. The measured binding energy values are in very good agreement with the reported literature values (248.4 for W^{6+} for W $4d_{5/2}$) [67].

3.3.3 TGA

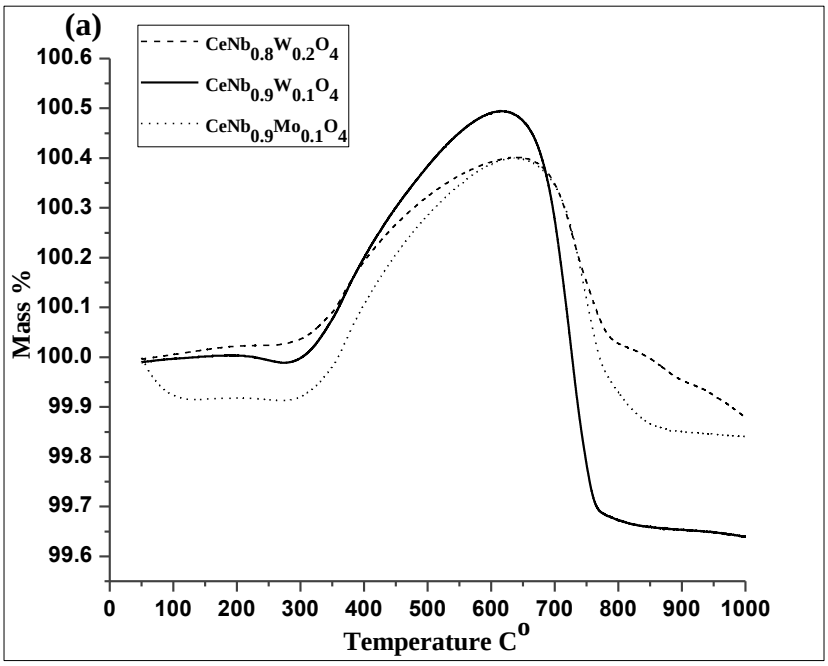

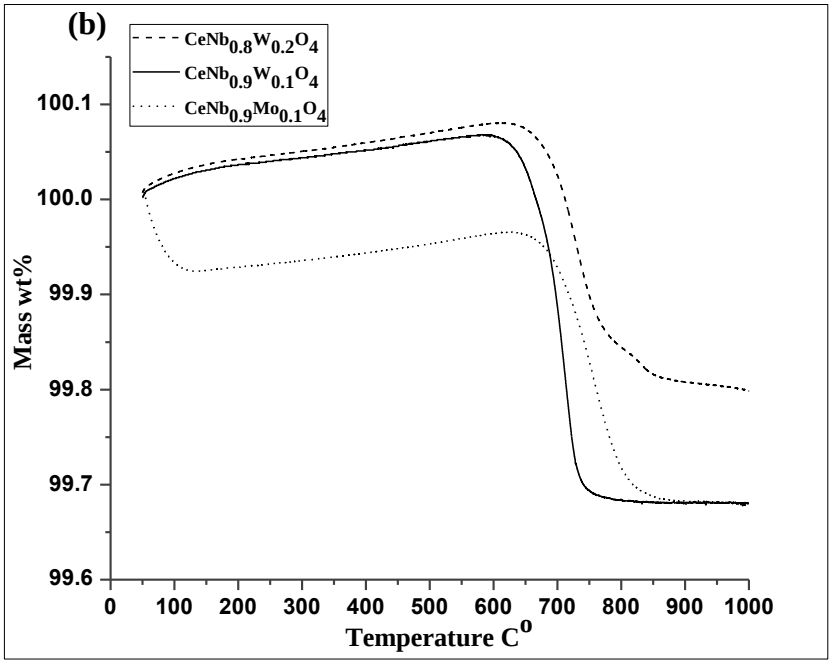

Figure 18. TGA data on heating from 50°C to 1000°C. (a) TPO of $CeNb_{0.9}W_{0.1}O_4$ $CeNb_{0.8}W_{0.2}O_4$ and $CeNb_{0.9}Mo_{0.1}O_4$, (b) TPR of $CeNb_{0.9}W_{0.1}O_4$, $CeNb_{0.8}W_{0.2}O_4$ and $CeNb_{0.9}Mo_{0.1}O_4$

It has been reported that the $CeNbO_{4+\delta}$ experiences a 0.6% increase in weight between 300 and 650^{o}C [50]. Figures 18(a) and 18(b) show the TPO and TPR behavior of $CeNb_{0.9}W_{0.1}O_4$, $CeNb_{0.8}W_{0.2}O_4$ and $CeNb_{0.9}Mo_{0.1}O_4$. From the data, it was calculated that $CeNb_{0.9}W_{0.1}O_4$ $CeNb_{0.8}W_{0.2}O_4$ and $CeNb_{0.9}Mo_{0.1}O_4$, gained a mass of up to 0.5, 0.46 and 0.3% respectively losing this weight upon reduction between 300 and 750^{o}C as seen in Figure 18(b) which is comparable to $CeNbO_{4+\delta}$. This occurs due to the interstitial vacancies formed as a result of changing elemental valence states mainly by Ce followed by a series of changes in the valence states of Nb and W as analyzed by XPS. Hence all the compositions under study experience an increase in mass which they lose upon reduction, showing the reversible mechanical nature of these compositions under redox and thermal cycling. Similar behavior was observed in A-site La doped $CeNbO_{4+\delta}$ [68]. In the case of the Mo substituted compound, only 0.3% mass gain is detected due to the fact that Mo substitution was not successful and this led to an increase in the reduced chemical state of Nb, thereby decreasing its amount which was compensated by the increase in the Ce^{4+} up to 18 at% (refer to Table 2) as analyzed by XPS.

3.3.4 Dilatometry

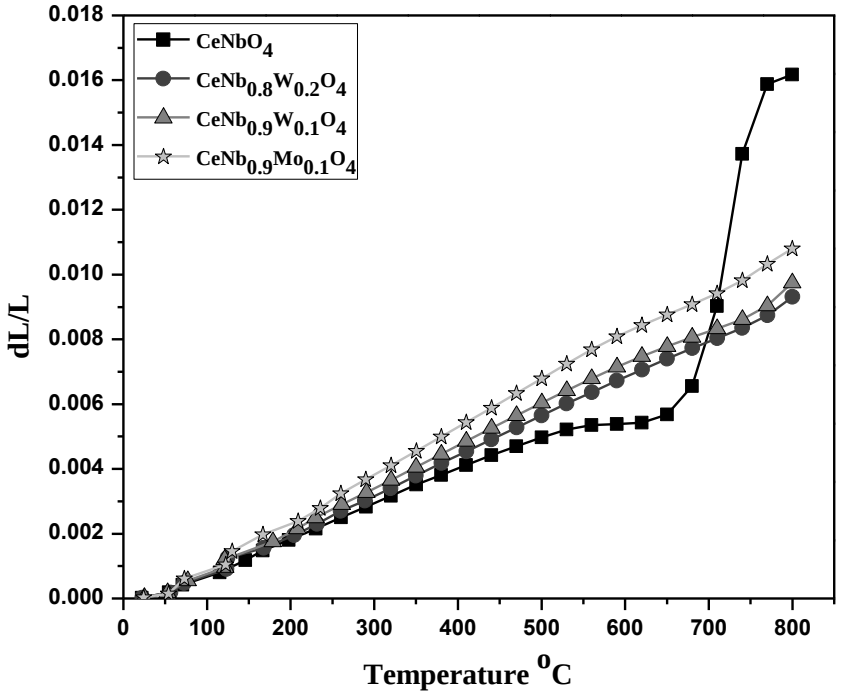

Figure 19. Dilatometry analysis of $CeNbO_{4+\delta}$, $CeNb_{0.9}W_{0.1}O_4$, $CeNb_{0.8}W_{0.2}O_4$ and $CeNb_{0.9}Mo_{0.1}O_4$ performed

Figure 19 shows the thermal behavior of the $CeNbO_{4+\delta}$, $CeNb_{0.9}W_{0.1}O_4$, $CeNb_{0.8}W_{0.2}O_4$ and $CeNb_{0.9}Mo_{0.1}O_4$ observed during the dilatometry study conducted in air. $CeNb_{0.9}W_{0.1}O_4$, $CeNb_{0.8}W_{0.2}O_4$ and $CeNb_{0.9}Mo_{0.1}O_4$ exhibits a smooth and linear thermal behavior up to 800^{o}C, whereas $CeNbO_{4+\delta}$ experiences a volumetric reduction at 600^{o}C followed by a rapid volumetric expansion at 650-700^{o}C due to the uptake of oxygen. This can be attributed to the change in valence state of cerium from Ce^{3+} to Ce^{4+} for which Ce^{4+} has smaller ionic radii compared to Ce^{3+} [50, 68]. But in the literature this volumetric transition has been reported to occur at 400^{o}C (volumetric reduction due to the formation of Ce^{4+}) and at 700-800^{o}C (volumetric expansion due to the formation of Ce^{3+}). The discrepancy can be due to the variation in the processing technique and the phase percentage of Monoclinic to Tetragonal present in the as-prepared compound. Skinner et al. [69] reported the complexity of redox chemical behavior in these material groups and concluded that the

valence change of Ce^{3+} to Ce^{4+} occurs at a higher rate than the reverse reaction. But in the current material systems under review, the B-site doping with a hexavalent material group, drastically reduced the kinetics of the Ce valence change and no noticeable volumetric expansion or reduction (Figure 19) is seen in these B-site doped $CeNbO_{4+\delta}$ under oxidizing condition. Table 4, lists the CTE of the $CeNbO_{4+\delta}$, $CeNb_{0.9}W_{0.1}O_4$, $CeNb_{0.8}W_{0.2}O_4$ and $CeNb_{0.9}Mo_{0.1}O_4$. It can be seen that the CTE of B-site doped $CeNbO_{4+\delta}$ can be compatible with YSZ8 ($10.826x10^{-6}$ K^{-1}) [70] and GDC20 (13.23 $x10^{-6}$ K^{-1}) [71], which are used as the electrolyte and barrier layer in a typical SOFC.

Table 4. The change in CTE with various B-site doping

Temperature Range (ºC)	**Material system**	**CTE ($x10^{-6}$ K^{-1})**
25-800	$CeNbO_{4+\delta}$	20.77 (average)
25-800	$CeNb_{0.9}W_{0.1}O_4$	12.85
25-800	$CeNb_{0.8}W_{0.2}O_4$	11.96
25-800	$CeNb_{0.9}Mo_{0.1}O_4$	13.6

Dilatometry was also performed to determine the thermomechanical redox behavior of $CeNbO_{4+\delta}$, $CeNb_{0.9}W_{0.1}O_4$, $CeNb_{0.8}W_{0.2}O_4$ and $CeNb_{0.9}Mo_{0.1}O_4$ at constant temperature of 800ºC.

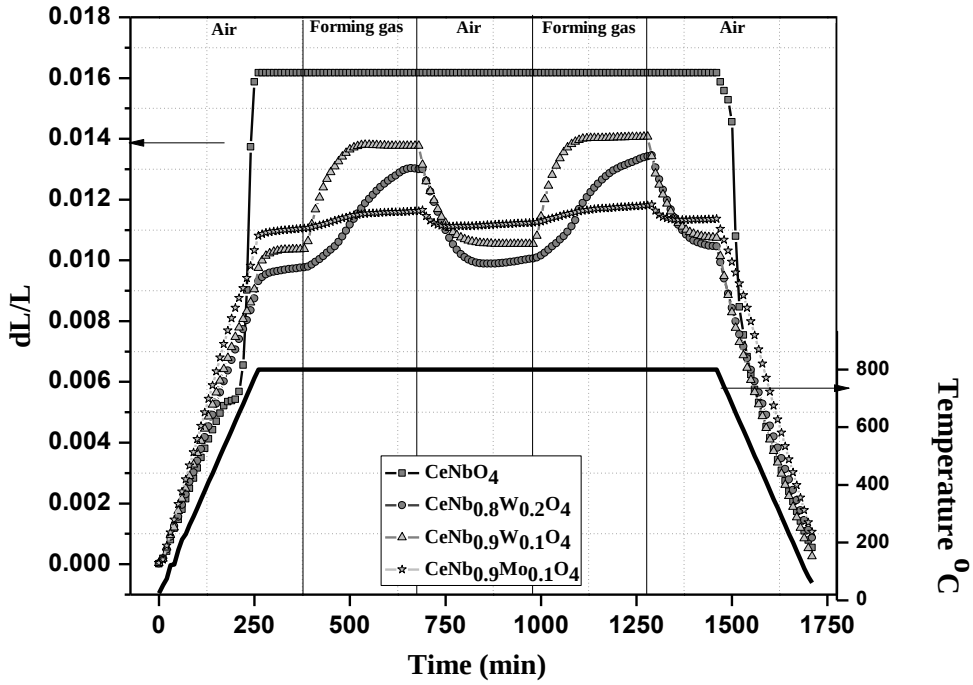

Figure 20. Redox behavior of $CeNbO_{4+\delta}$, $CeNb_{0.9}W_{0.1}O_4$, $CeNb_{0.8}W_{0.2}O_4$ and $CeNb_{0.9}Mo_{0.1}O_4$ at an isotherm of 800°C (2 redox cycles of 10 hours each)

The high temperature redox testing protocol used in this experimentation is as explained in Chapter 2, Figure 10. Segment 1-2: ramping up the temperature to 800°C at 3°C/min in air; Segment 2-3: Isothermal for 2 hours at 800°C for temperature stabilization; Segment 3-7: Isothermal for 20 hours at 800°C with automated atmospheric change from oxidizing to reducing, with each cycle performed for 10 hours; and Segment 7-8: ramping down the temperature to RT at 3°C/min in air.

As seen in Figure 20, the B-site doped compositions experience a volumetric expansion the in reducing atmosphere. As all the compositions are hyper stoichiometric, during reduction, in the case of doped compositions, they are reduced to their stoichiometric chemical state leading to oxide vacancies resulting in excess negative charge formation, thus causing expansion of the lattice. Similar behavior is seen in fluorite structured CeO_2, where lower valent gadolinium oxide is doped to limit the degree of expansion upon reduction [72]. It can be also observed from Figure 20 that the amount of doping effects the degree of reduction. For example $CeNb_{0.9}W_{0.1}O_4$ experiences a volumetric expansion

of 0.34% compared to $CeNb_{0.8}W_{0.2}O_4$ which expands about 0.3%. But when 10 mol% Mo is doped on the B-site ($CeNb_{0.9}Mo_{0.1}O_4$), the degree of expansion drops down to just 0.06%. Nevertheless the volumetric expansions exhibited by all the B-site doped compositions are reversible, at least up to two redox cycles. From the XPS quantification (refer Table 2) $CeNb_{0.8}W_{0.2}O_4$ has 24 atomic wt. % of interstitial oxygen whereas $CeNb_{0.9}Mo_{0.1}O_4$ has only 20 atomic wt. % of interstitial oxygen which upon reduction forms less interstitial vacant sites compared to $CeNb_{0.9}W_{0.1}O_4$ and $CeNb_{0.8}W_{0.2}O_4$. Hence one can conclude that the degree of expansion is also directly influenced by the amount of interstitials. The redox behavior is also influenced by the ratio of Ce^{3+} to Ce^{4+} present in the compounds. In the case of un-doped $CeNbO_{4+\delta}$ this ratio is 14.5, whereas $CeNb_{0.9}Mo_{0.1}O_4$ and $CeNb_{0.8}W_{0.2}O_4$ the Ce^{3+} to Ce^{4+} ratio is 4.55 to 3.17 respectively. Hence a higher Ce ratio results in greater redox stability. Therefore it can be seen from Figure 20 the un-doped $CeNbO_{4+\delta}$ is redox stable compared to the doped compositions and the Mo doped composition is relatively redox stable when compared to the W doped composition due to a higher Ce^{3+} to Ce^{4+} ratio.

3.3.5 Electrical conductivity

Figure 21(a) shows the conductivity of the un-doped and B-site doped $CeNbO_{4+\delta}$ in an oxidizing atmosphere. The un-doped $CeNbO_{4+\delta}$ recorded a maximum conductivity of about 0.12 S/cm at 650^{o}C compared to remaining B-site doped compositions. With further increase in temperature the conductivity drops to 0.043 S/cm at 800^{o}C. This can be explained due to the phase transition which is observed at the temperature range of 600^{o}C, where the un-doped $CeNbO_{4+\delta}$ experiences a volumetric reduction and rapidly expands in the 650-750^{o}C range owing to oxygen uptake as observed from the dilatometry study (Figure 19). Skinner et al. reported a conductivity of 0.03 S/cm [55] at 850^{o}C. The conductivity of $CeNbO_{4+\delta}$ reported in this work can be compared to $CeVO_{4+\delta}$ (0.042 S/cm at 850^{o}C) [73]. The B-site doped $CeNb_{0.9}W_{0.1}O_4$, $CeNb_{0.8}W_{0.2}O_4$ and $CeNb_{0.9}Mo_{0.1}O_4$ exhibit a linear electrical conductivity which increases with temperature like any other semi-conducting material. As seen in Figure 21(a) $CeNb_{0.9}W_{0.1}O_4$, $CeNb_{0.8}W_{0.2}O_4$ and $CeNb_{0.9}Mo_{0.1}O_4$ recorded a maximum total conductivity of 0.082, 0.031 and 0.05 S/cm at 800^{o}C respectively.

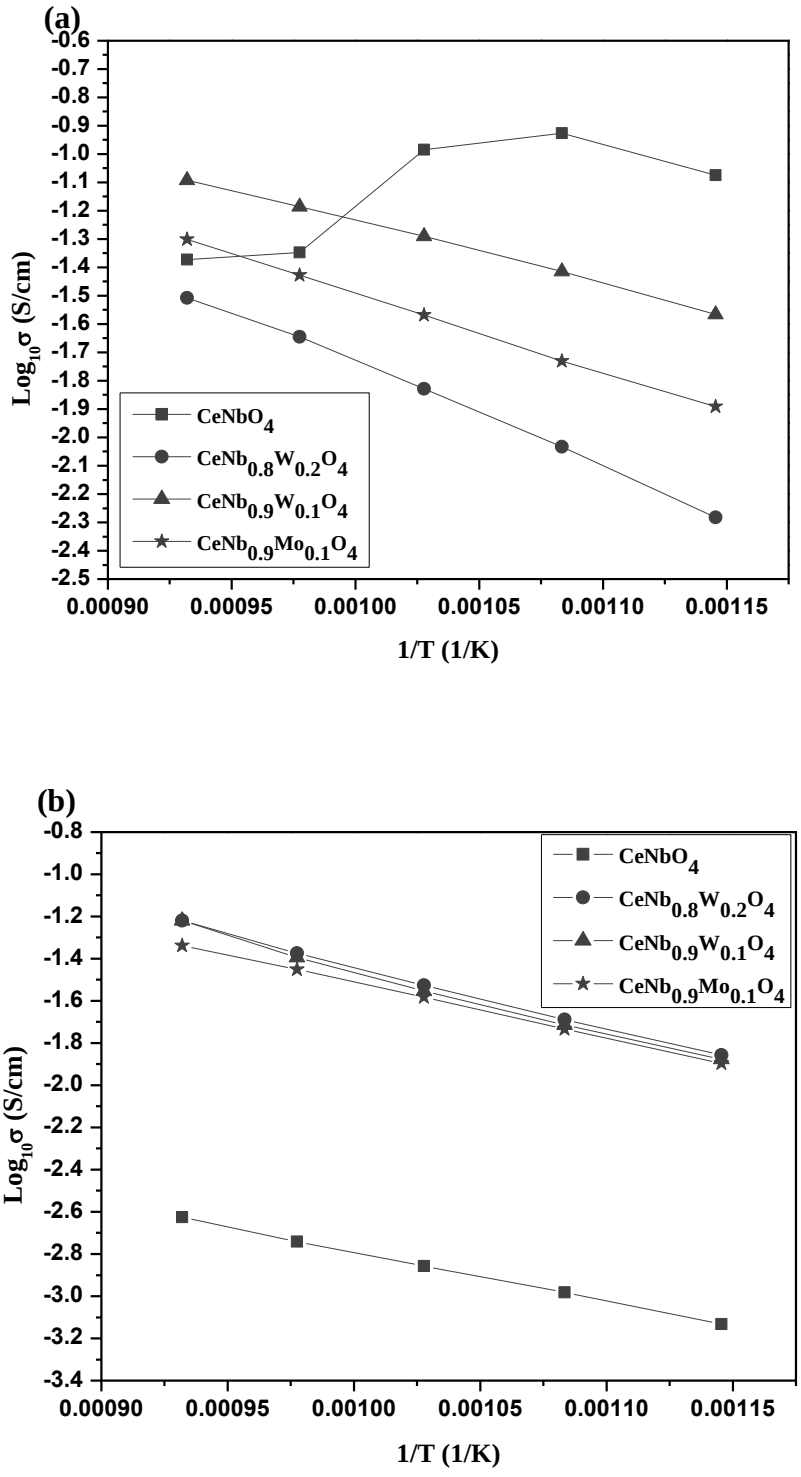

Figure 21. Electrical conductivity of $CeNbO_{4+\delta}$, $CeNb_{0.9}W_{0.1}O_4$, $CeNb_{0.8}W_{0.2}O_4$ and $CeNb_{0.9}Mo_{0.1}O_4$ between 25 – 800ºC. (a) Electrical measurement performed in air, (b) Electrical measurement performed in forming gas

It can be observed that the total electrical conductivity decreases with higher doping content owing to the fact that higher mol % doping decreases the interstitial oxygen, which can be related to the higher CTE of $CeNb_{0.9}W_{0.1}O_4$ compared to $CeNb_{0.8}W_{0.2}O_4$ (refer Table 4).

Figure 21(b) is the total electrical conductivity of the compositions in reducing atmosphere. It is interesting to see how the total conductivity of the un-doped $CeNbO_{4+\delta}$ decreases from 0.043 S/cm to 0.002 S/cm when the atmosphere is starved from oxygen, indicating, though $CeNbO_{4+\delta}$ is a mixed conductor, it is mainly an ionic conductor. Also the B-site doped composition recorded similar conductivity values in both gaseous atmospheres. The doping of hexavalent (W^{6+}) on the pentavalent (Nb^{5+}) site makes the material an n-type conductor, which was the intent of the doping strategy adopted in this work. But it is worth noting the existence of various valence states of W (W^{6+}, W^{5+} and W^{4+}) in the $CeNb_{0.9}W_{0.1}O_4$, $CeNb_{0.8}W_{0.2}O_4$ compositions which give rise to electron holes making it a mixed p and n-type conductor. Similar behavior is observed when vanadium is substituted in the B-site of $CeNbO_{4+\delta}$ [50]. Further work is needed to distinguish the amount of p-type, n-type and ionic conductivity from the total electrical conductivity.

3.4 Conclusion

B-site doping of $CeNbO_{4+\delta}$ with hexavalent W and Mo has been undertaken in an attempt to make the material a mixed ionic and electronic conductor for SOFC anode applications. Up to 20 mol % W and 10 mol % Mo was doped confirming the formation of biphasic Monoclinic I2/a and Tetragonal $I4_1/a$ crystal structures from XRD at room temperature. XPS analysis at room temperature confirmed the successful substitution of W in Nb-site and the local effects of the W^{6+} oxidation state. XPS revealed the increase in Ce^{4+} with the doping of both Mo and W. However Mo substitution was not successful which led to the increase in the reduced chemical state of the Nb compensated by the increase in the Ce^{4+} up to 18 at%. From the dilatometry study in air, it was demonstrated the B-site doped composition made the parent material mechanically stable up to 800^{o}C, seizing the structural change generally observed in $CeNbO_{4+\delta}$ scheelite material group at elevated temperature. Though the B-site doped compositions demonstrated a volumetric expansion upon redox dilatometry, it is worth mentioning these volumetric changes are reversible

thus proving the thermomechanical redox stability induced upon B-site doping. The total electrical conductivity in air and reducing atmosphere confirms un-doped $CeNbO_{4+\delta}$ is mainly an ionic conductor with no noticeable change in total electrical conductivity in B-site doped $CeNbO_{4+\delta}$ irrespective of the experimental atmosphere. Though the conductivity value is not as good as typical SOFC NiO/YSZ [74] anode material, the doped $CeNbO_{4+\delta}$ is highly redox stable unlike NiO/YSZ. Further work needs to be undertaken to improve the total conductivity of these compositions along with a determination of the individual contributions to the total electrical conductivity.

Chapter 4. Thermo-Mechanical Redox Stability Analysis of Nb_2TiO_7 and $Nb_{1.33}Ti_{0.67}O_4$ for SOFC Application

4.1 Introduction

Solid Oxide Fuel Cells (SOFCs) are capable of working with high efficiencies in a range of fuels. Light hydrocarbon fuels can be directly used through internal reforming or direct oxidation. Hence the SOFC can be one of the answers for upcoming fuel cell technology based on current economic trends. Due to the outstanding electrochemical performance at reduced operating temperature (600-800^{o}C) the anode-supported cell has a remarkable prospect with respect to commercialization [75]. The state-of-the-art Ni/YSZ cermet is an excellent catalyst for fuel oxidation and also an effective current collector. But it has poor mechanical stability during Reduction and Oxidation cycles (redox), experiencing an irreversible volumetric change of about 2.5% [76]. The cermet's degradation is mainly due to irreversible microstructural changes resulting in an increased polarization resistance with each redox cycle. Hence the development of redox stable anode materials is a well-focused research area in SOFC fraternity.

There are various reports on the development of redox stable anode materials, suggesting that the material development has been under consideration for several years now. A number of interesting compositions have been identified in recent years, notably double perovskite like $Sr_2Mg_{1-x}Mn_xMoO_{6-\delta}$ [77]. Here Mn enhances the electrochemical reaction and as an electro-catalyst, it reduces the overpotential when coated on the YSZ electrolyte [78] and perovskites like Y substituted $SrTiO_3$ [79] known for its high mechanical redox stability. These materials are generally known as Mixed ionic-electronic conductors (MIEC) as they exhibit both ionic and electronic conduction at elevated temperatures thus avoiding the need of composite anodes like Ni/YSZ. MEIC have potential applications as SOFC electrodes, syngas production reactor membranes and oxygen separation membranes.

In the past, MEIC materials with the composition $A_{0.6}M_xNb_{1-x}O_{3-\delta}$ (A = Ba, Ca, La, Sr and M = Cr, Fe, Mn, Mg, Ni, In, Sn) [80, 81] have been considered for the SOFC anode. During this study to develop phase stable and mechanically stable anode, Nb_2O_5 impurity was identified. But when Nb_2O_5 was reduced to NbO_2, it exhibited good electronic conduction.

Since then, Nb based rutile structures have been considered as an alternative SOFC anode material. Unlike Ni, Nb is a non-tonic and non-carcinogenic metal which can replace Ni is applications like steam electrolysis. Reich et al. [82] investigated Nb_2TiO_7 based rutile material and found that at SOFC operating temperatures of 800^oC and above, Nb_2TiO_7 reduced to $Nb_{1.33}Ti_{0.67}O_4$ in reducing atmosphere. $Nb_{1.33}Ti_{0.67}O_4$ has a high electronic conductivity of about 100 S/cm^{-1} and a very low thermal expansion coefficient of 3 x 10^{-6} K^{-1}. Due to the high electrical conductivity, it was suggested as a good current collector. Li et al. used Nb_2TiO_7 as a redox-reversible cathode for direct high-temperature steam electrolysis and indicated that Nb_2TiO_7 can be a good candidate for the fuel cell electrode [83]. But none of these studies mention the mechanical redox stability of the material, which is critical for a SOFC anode material.

In this Chapter, a thorough investigation into the mechanical redox stability of both Nb_2TiO_7 and $Nb_{1.33}Ti_{0.67}O_4$ is reported to evaluate the primary readiness of the material as a SOFC anode. Both the compositions were separately synthesized and their mechanical redox stability was evaluated using a redox dilatometry technique at 800^oC. Also the change in electrical conductivity during redox cycling at 800^oC has been evaluated for both the material compositions individually. The difference in the microstructure of both the compositions has also been investigated in the current paper.

4.2 Experimental

Powder samples of Nb_2TiO_7 and $Nb_{1.33}Ti_{0.67}O_4$ were prepared via a solid-state synthesis technique using Nb_2O_5 (Aldrich, 99.9%) and MoO_3 (Alfa Aesar, 99.5% min). Both the precursor powders were stoichiometrically mixed in an attrition mill for 4 h in ethanol using 2 mm size zirconia milling media. The milled precursor mixture was then air dried at 80^oC for 24 h and calcined at 1450^oC for 5 hours in air to obtain Nb_2TiO_7. To obtain a pure phase of $Nb_{1.33}Ti_{0.67}O_4$, calcined Nb_2TiO_7 powder was attrition milled and dried similar to above mentioned manner. The milled Nb_2TiO_7 powder was calcined in 5%H_2/95%N_2 reducing atmosphere for 5 h at 1450^oC to obtain a single-phase reduced Nb_2TiO_7 in the form of $Nb_{1.33}Ti_{0.67}O_4$. Phase purity of the powder sample was analyzed using a PANalytical X'Pert Pro X-ray diffractometer with Cu-$K_{\alpha1}$ of 1.5406 Å wavelength. The thermomechanical redox stability of the material was studied using the NETSZCH DIL 402C dilatometer. Compressed air was used for the oxidizing atmosphere and forming

gas (5% H_2 - 95%N_2) was used for the reducing atmosphere. A sapphire standard was used to calibrate the dilatometer before all dilatometry tests. Electrical characterization was carried out using a DC 4-point probe technique using a Keithley 2100 digital multimeter in both oxidizing (compressed air) and reducing atmosphere (forming gas: 5%H_2-95%N_2). All the electrical measurements were taken between 25 – 800ºC. The microstructure of the test samples was analyzed using the Hitachi S-4700 SEM.

4.3 Results and discussion

Figure 22 shows the XRD analysis of the as-synthesized Nb_2TiO_7 calcined in air at 1450ºC for 5 hours and $Nb_{1.33}Ti_{0.67}O_4$ calcined in forming gas at 1450ºC for 5 hours. The phases were matched with PDF card 01-077-1374 for Nb_2TiO_7 and PDF card 00-053-0293 for $Nb_{1.33}Ti_{0.67}O_4$ to confirm the phase purity as seen in Figure 22. As mentioned in the section 4.1, though Nb_2O_5 and its reduced form NbO_2 exhibit good electronic conductivity, it has been reported that pure Nb_2O_5 deforms in shape and disintegrates during the sintering process. Here the addition of TiO_2 to Nb_2O_5 greatly improves the sinterability and provides good mechanical properties compared to Nb_2O_5 [82]. Nb_2TiO_7 has a monoclinic structure crystalizing in the C2/m space group (a (Å) = 20.3510, b (Å) = 3.8010 and c (Å) = 11.8820). $Nb_{1.33}Ti_{0.67}O_4$ has a tetragonal structure crystalizing in the P42/mnm space group (a (Å) = 4.7564, b (Å) = 4.7564 and c (Å) = 2.9983). There is a considerable reduction in the lattice parameter (23% by volume) owing to the change in crystal structure upon reduction of Nb_2TiO_7 into $Nb_{1.33}Ti_{0.67}O_4$. This can also suggest that reduction induces a considerable amount of strain in this material system. Reich et al. [82] reported that Nb_2TiO_7 they obtained crystalized in I2/m space group with a monoclinic crystal structure (a (Å) = 11.9, b (Å) = 3.77 and c (Å) = 10.1). The discrepancy in the crystal system as well as the lattice parameters are yet to be known. Whereas Li et al. [83] and Lashtabeg et al. [84] report conforms to the crystal structure and lattice parameter reported in this work for both Nb_2TiO_7 and $Nb_{1.33}Ti_{0.67}O_4$.

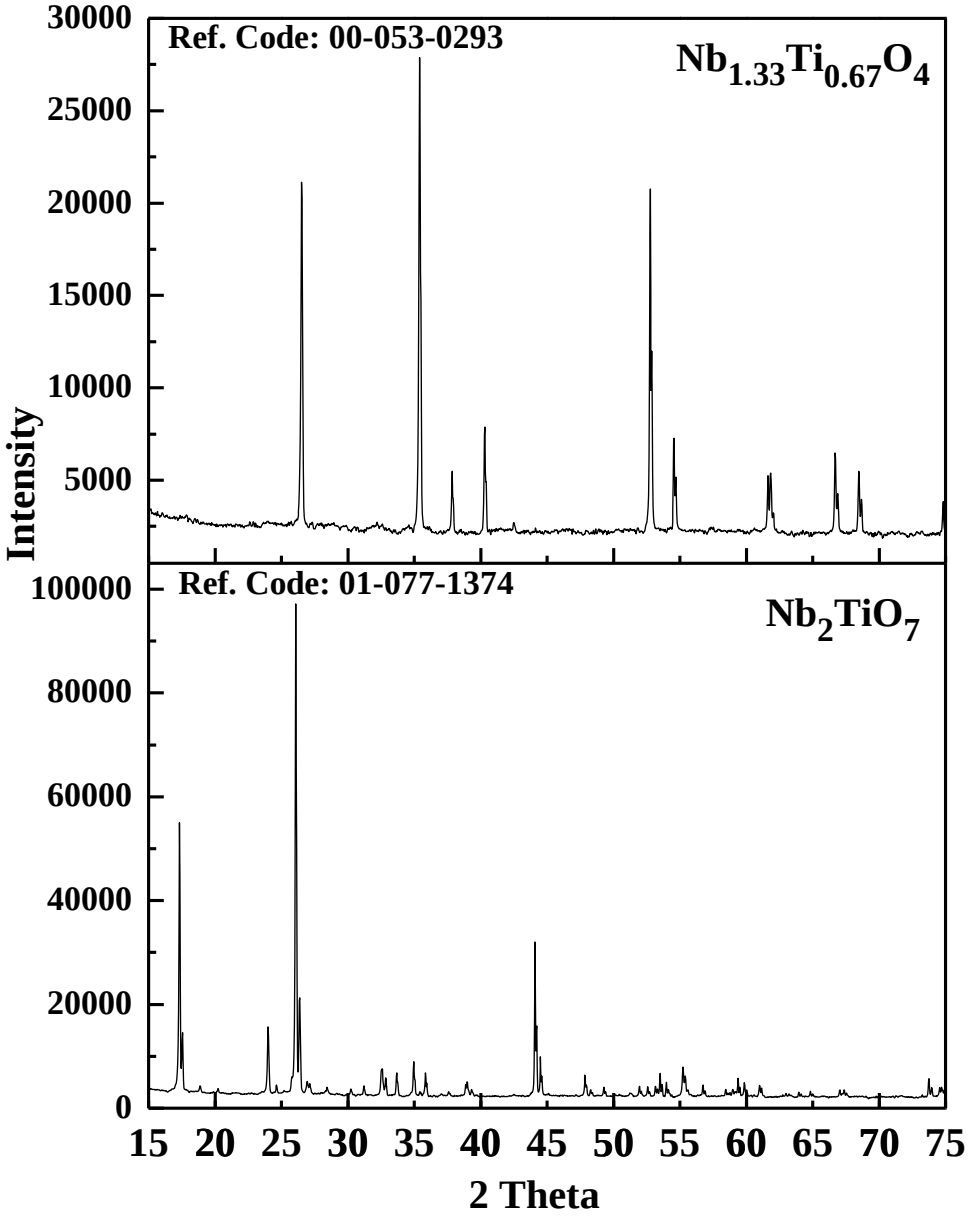

Figure 22. XRD spectrum of Nb_2TiO_7 (bottom) and $Nb_{1.33}Ti_{0.67}O_4$ (top)

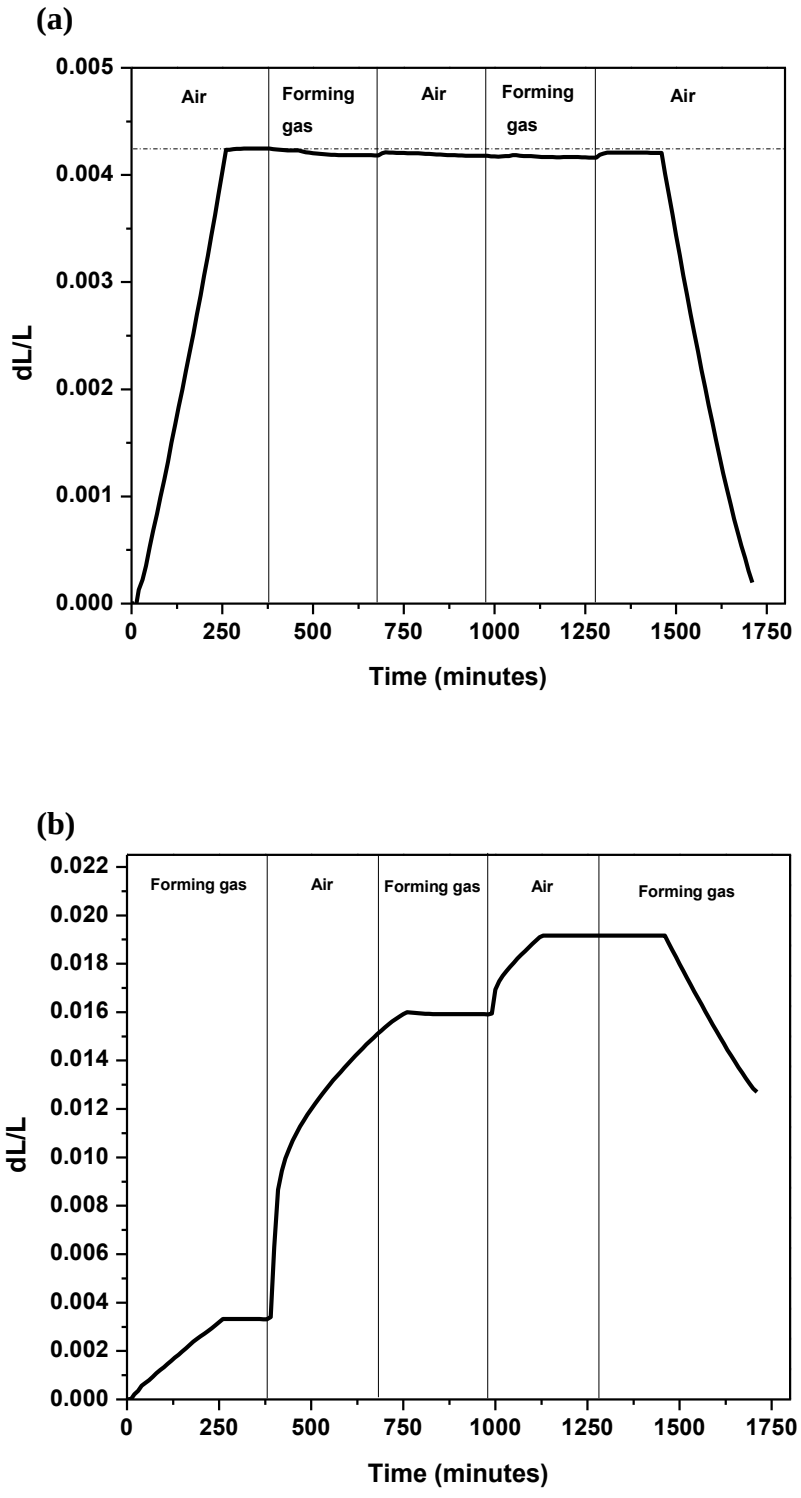

Figure 23. High temperature redox dilatometry graphs. (a) Nb_2TiO_7 bulk sample, (b) $Nb_{1.33}Ti_{0.67}O_4$ bulk sample

Figure 23 is the high-temperature redox dilatometry of Nb_2TiO_7 (Figure 23a) and $Nb_{1.33}Ti_{0.67}O_4$ Figure 23b). Bulk bar samples of 25 mm in length and 2.5 mm in width and thickness as shown in Chapter 2, Figure 9, were used for both the dilatometry and electrical conductivity tests. The bulk Nb_2TiO_7 sample had a relatively density of 88% when sintered at 1400^{o}C for 2 hours in air and the bulk $Nb_{1.33}Ti_{0.67}O_4$ had a relatively density of 80% when sintered at 1400^{o}C for 2 hours in forming gas. The dilatometry test protocol is as shown in Chapter 2, Figure 10: Each sample was heated to 800^{o}C at 3^{o}C/min in the atmosphere in which they were sintered and held at 800^{o}C for 2 hours (for temperature stabilization) before 2 redox cycles of 10 hours each (each reduction and oxidation cycles performed for 5 hours) at 800^{o}C. The samples were then brought back to room temperature at 3^{o}C/min in the atmosphere, which they were sintered. As seen in Figure 23a Nb_2TiO_7 exhibits good redox stability at 800^{o}C with a minimum volumetric reduction of around 0.006% in reducing atmosphere, which is reversible in nature. As claimed by other researchers [82-84], Nb_2TiO_7 exhibits high mechanical redox stability at SOFC operating temperature of 800^{o}C. It has a CTE of 5.46 x 10^{-6} K^{-1} in air between 25-800^{o}C, which is far less than YSZ. This is the first time the mechanical redox behavior of Nb_2TiO_7 has been reported. Li et al. [83] in their work only demonstrate the chemical redox stability of Nb_2TiO_7 and $Nb_{1.33}Ti_{0.67}O_4$ and claim to be a good electrode material. But mechanical redox stability is more important as poor mechanical redox instability can compromise the integrity of the fuel cell causing cracks and leaks. Figure 23b is the redox dilatometry of $Nb_{1.33}Ti_{0.67}O_4$. It has a CTE of 4.25 x 10^{-6} K^{-1} in forming gas between 25-800^{o}C. One of the reasons for the decrease in CTE compared to Nb_2TiO_7, is the difference in the relative densities of the test samples. When the material oxidizes to Nb_2TiO_7 in the first oxidation cycle, there is a drastic volumetric expansion of up to 1.3% comparable to NiO/YSZ [76]. The expansion only plateaus upon the introduction of reducing gas as seen in Figure 23b. But it has to be noted that, the volumetric change is irreversible in nature and cracked the test sample after the second oxidation cycle. The material experienced a total of 1.9% irreversible volumetric expansion over two redox cycles. The reason for this drastic volumetric expansion is the oxidation of $Nb_{1.33}Ti_{0.67}O_4$ into Nb_2TiO_7 which increases the unit cell volume by 23% as mentioned earlier [85].

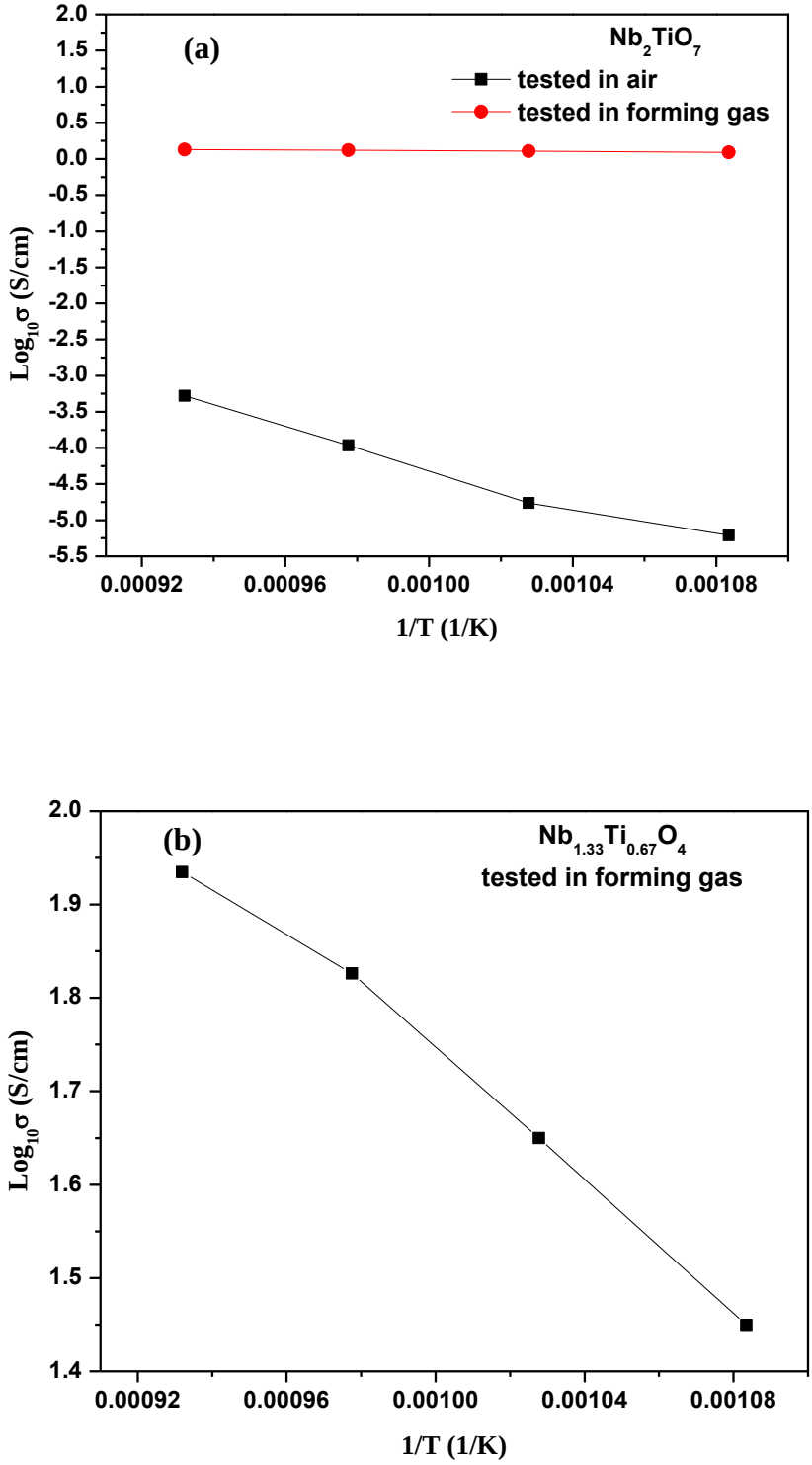

Figure 24. DC four-point electrical conductivity data. (a) Nb2TiO7 bulk sample, (b) Nb1.33Ti0.67O4 bulk sample

Figure 24 is the Four point DC electrical conductivity of Nb_2TiO_7 (Figure 24a) performed in air and forming gas and $Nb_{1.33}Ti_{0.67}O_4$ (Figure 24b) performed in forming gas only as $Nb_{1.33}Ti_{0.67}O_4$ is mechanically not stable in air as observed by redox dilatometry test. Nb_2TiO_7 is a p-type conductor. For Nb_2TiO_7, Li et al. [83] has reported a DC electrical conductivity between 10^{-7} to 10^{-3} S/cm at 800ºC in air. From Figure 24a, Nb_2TiO_7 has an initial conductivity of 10^{-5} S/cm at 650ºC which increase to 10^{-3} S/cm at 800ºC in air. Lashtabeg et al. [84] also reported a conductivity of 1.7 x 10^{-3} S/cm at 900ºC in air. In forming gas the conductivity of Nb_2TiO_7 increases to 1.35 S/cm in the temperature range 650-800ºC as seen in Figure 24a. In contrast $Nb_{1.33}Ti_{0.67}O_4$ is an n-type conductor, where the conductivity is due to the edge sharing octahedral along the c-axis [86]. Fontaine et al. [87] and Darlinski et al. [88] reported that in Nb_2TiO_7, only the Nb^{5+} valence state is observed. However in $Nb_{1.33}Ti_{0.67}O_4$, Fontaine et al. [87] and Bahl et al. [89] reports that Nb^{5+} partially reduces to Nb^{4+} favoring the formation of a Nb-Nb metal bond, thus facilitating high electronic conductivity of $Nb_{1.33}Ti_{0.67}O_4$ in a reducing atmosphere. In the present work, as seen in Figure 24b, $Nb_{1.33}Ti_{0.67}O_4$ exhibits a high electronic conductivity of 85 S/cm at 800ºC in forming gas. Lashtabeg et al. [84] reported a conductivity in excess of 120 S/cm at 900ºC in 5% H_2/Ar, whereas Li et al. [83] reported a conductivity as low as 49 S/cm at 800ºC in 5% H_2/Ar for $Nb_{1.33}Ti_{0.67}O_4$. The discrepancy in the value of conductivities may be due to the initial purity of the precursors, difference in relative density of the test sample and also due to different grain size and grain boundary defects. Nevertheless the study has pointed out, how the starting chemical composition of NbTO plays a crucial role in redox mechanical stability as well as electronic conductivity of the material. Due to the extrinsic and intrinsic complications of the material properties, single phase Nb_2TiO_7 as a starting composition is not an ideal anode candidate for SOFC applications. However compositing Nb_2TiO_7 with materials like $Gd_{0.1}Ce_{0.9}O_2$ can enhance its conductivity and catalytic properties for SOFC application. If $Nb_{1.33}Ti_{0.67}O_4$ is used as the starting anode composition, adopting different B site doping strategies to increase the unit cell volume to match the unit cell volume of Nb_2TiO_7 can be a feasible approach to use $Nb_{1.33}Ti_{0.67}O_4$ as an SOFC anode. Also the range of conductivity demonstrated by Nb_2TiO_7 in high pO_2 and low pO_2 atmospheres makes it suitable as a gas sensor that exhibits a change in resistivity of the material due to gas adsorption.

4.4 Conclusion

The $Nb_{1.33}Ti_{0.67}O_4$ composition was previously suggested as a promising alternative for NiO/YSZ anode in SOFC applications. The present study showed that $Nb_{1.33}Ti_{0.67}O_4$ could be formed during reducing calcination and the material possessed a relatively high electronic conductivity of 85 S/cm at 800^{o}C in a reducing atmosphere. Unfortunately, the material exhibited poor thermo-mechanical redox stability, expanding irreversibly up to 1.9% when oxidized, and ultimately the material irreversibly cracked during atmosphere cycling. In the case where Nb_2TiO_7 is the starting composition, this material exhibited high thermo-mechanical redox stability, but displayed poor electronic conductivity at 800^{o}C. Both materials also demonstrated a low CTE value far below that of YSZ, the typical electrolyte utilized for SOFCs. Hence, these materials in their true form cannot be used in SOFC anode applications. Nevertheless many doping strategies can be adopted to improve the redox stability of $Nb_{1.33}Ti_{0.67}$ to make it a potential anode material. From this work, it can be noted that simple high-temperature dilatometry testing can act as a powerful tool in the material development process.

Chapter 5. Effect of Mg/Mo Ratio in a Stoichiometric $Sr_2MgMoO_{6-\delta}$ (SMM) Redox-Stable Anode

5.1 Introduction

The SOFC anode material must act as a catalyst for hydrogen and/or hydrocarbon oxidation, which includes efficient fuel adsorption, ionic/electronic charge transfer, and electronic conduction. An ideal SOFC anode should be an excellent mixed oxide-ion-electron conductor (MIEC). Tao et al. [90, 91] reported that the $(La_{1-x}Sr_x)_{0.9}Cr_{0.5}Mn_{0.5}O_{3-\delta}$, a MIEC anode, showed good catalytic activity for the electro-oxidation of methane at elevated temperature. Its performance was comparable with Ni/YSZ, but like Ni/YSZ it exhibited poor sulphur tolerance. However this study helped with the introduction of mixed valent and MIEC double perovskites ($A_2BB'O_{6-\delta}$) into the SOFC research fraternity. Early work on double perovskite $Sr_2MgMoO_{6-\delta}$ (SMM) showed it offers excellent performance as a SOFC anode, with acceptable chemical stability, MIEC, electro-catalytic activity and resistance to poisoning by sulphur in the fuel [92, 93]. This oxide also has a CTE comparable to the YSZ electrolyte. Hence, in the current study this material is further investigated in more detail to evaluate its key features like thermal redox stability and thermal redox electronic conductivity. SMM possesses the double-perovskite structure, with a tetragonal lattice at room temperature due to octahedral tilting [93], but for unit cell refinement and quantitative analysis a pseudo-cubic cell can be considered. In SMM, the extent to which the structure becomes oxygen deficient upon reduction, creates anionic vacancies and allows for a level of ionic conduction. The reduction of Mo^{6+} to Mo^{5+} generates an electronic carrier, thus making SMM a MIEC. In many double-perovskites, the extent of ordering (B/B' ratio) largely affects its physical properties. For example in the case of $Sr_2FeMoO_{6-\delta}$, a half-metallic ferrimagnetism is exhibited in an ordered phase and this property diminishes as the ordering between B and B' decreases [94]. In the current chapter, the effect of the ratio of Mg/Mo on the physical properties was compared with the stoichiometric SMM (Mg/Mo = 1). The detailed thermal redox behavior of the $Sr_2MgMoO_{6-\delta}$ and $Sr_2Mg_{1-x}Mo_{1+x}O_{6-\delta}$ (x = 0.1 and 0.2) was studied and the systematic development of stoichiometric SMM to a redox stable SMM is reported in this Chapter.

5.2 Experimental

Powder samples of the $Sr_2MgMoO_{6-\delta}$ and $Sr_2Mg_{1-x}Mo_{1+x}O_{6-\delta}$ (x = 0.1 and 0.2) were prepared via a solid-state synthesis route using $SrCO_3$ (Alfa Aesar, 97.5%), MO_3 (Alfa Aesar, 99.5% min) and MgO (Alfa Aesar, 96%). All the above chemical compounds were stoichiometrically mixed in an attrition mill for 4 h using zirconia milling media in ethanol for 4 h. The milled mixture was dried at 80^{o}C for 24 h and heat treated to 1000^{o}C in air for 4 h to eliminate carbonates. The heat-treated powder was again attrition milled for 4 h in ethanol and the dried powder was calcined in forming gas (5%H_2/95%N_2) at 1300^{o}C for 4 h. The calcination process was repeated twice in total to obtain phase purity. Phase purity was analyzed using a PANalytical X'Pert Pro X-ray diffractometer with Cu-$K_{\alpha 1}$ of 1.5406 Å wavelength. For dilatometry and electrical conductivity tests, ~8.5 grams of the phase pure powder was uniaxially pressed at room temperature into a cylindrical pellet of 30 mm in diameter and 2.5 mm thick and sintered at 1300^{o}C for 2 h in forming gas. The thermomechanical redox stability of the material was studied using the NETSZCH DIL 402C dilatometer. Four-4 point DC total electrical conductivity measurement with a constant current of 20 mA was used for electrical characterization. Four notches were cut on the bar samples and platinum wire was wound in the notch secured by platinum paste. All the conductivity measurements were taken between 25 – 800^{o}C temperature range using a Keithley 2100 digital multimeter in both oxidizing (compressed air) and reducing atmospheres (forming gas).

5.3 Results and discussion

5.3.1 XRD analysis of the SMM powder

From the XRD pattern in Figure 25, the phase purity of $Sr_2MgMoO_{6-\delta}$ can be confirmed. A bar sample (25 mm *x* 2.5 mm *x* 2.5 mm) of this phase pure powder was sintered as mentioned in the experimental section 5.2 for redox dilatometry and 4-point DC electrical characterization. From those analyses, it was revealed that the stoichiometric SMM composition, though thermally redox stable (explained in the later sub-section), failed to satisfy electrical redox stability at 800^{o}C, the typical SOFC operating temperature. Hence to make the composition both thermally and electrically redox stable, the B/B'-site ratio of the SMM was varied accordingly: $Sr_2Mg_{1-x}Mo_{1+x}O_{6-\delta}$, where x = 0.1 and 0.2. At 0.2 mol% Mo, the XRD analysis revealed the inclusion of MoO_3 precursor which failed to enter the

SMM matrix. Hence 0.2 mol% was found to be the threshold for excess Mo addition as seen in Figure 26. Mo content was increased as it is a known that for the SMM system to obtain the electrical conductivity, surplus generation of Mo^{5+} is a pre-requisite. Another possible route to improve the conductivity is to increase the oxygen deficiency. It has been reported that the maximum obtainable deficiency was near $\delta = 0.046$ via the solid-state synthesis process [95]. Hence altering the B-site ratio is more logical and was employed in this study. Figure 26, shows the XRD pattern of SMM synthesized with different Mg/Mo ratios. In this study, SMM with excess Mo ($Sr_2MgMo_{1.1}O_{6-\delta}$) in the stoichiometric ($Sr_2MgMoO_{6-\delta}$) composition was also considered to see how it affected the redox stability compared to other compositions as seen in Figure 26. XRD analysis of $Sr_2MgMo_{1.1}O_{6-\delta}$ (refer Figure 26) also showed the inclusion of MoO_3 as in the $Sr_2Mg_{0.8}Mo_{1.2}O_{6-\delta}$ composition. Further addition of Mo was not considered.

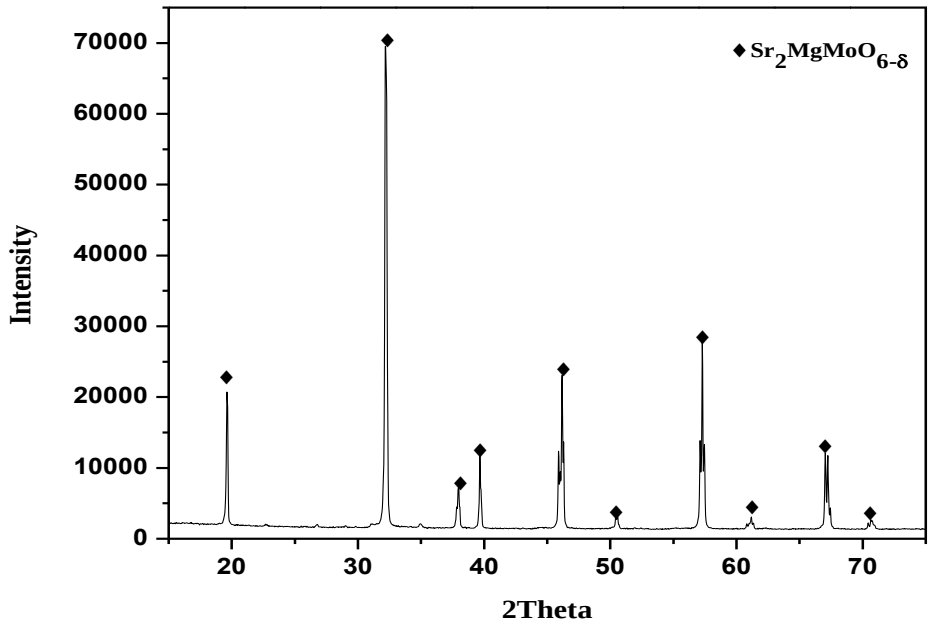

Figure 25. XRD pattern of the stoichiometric $Sr_2MgMoO_{6-\delta}$ prepared via solid state synthesis and calcined in forming gas at 1300ºC

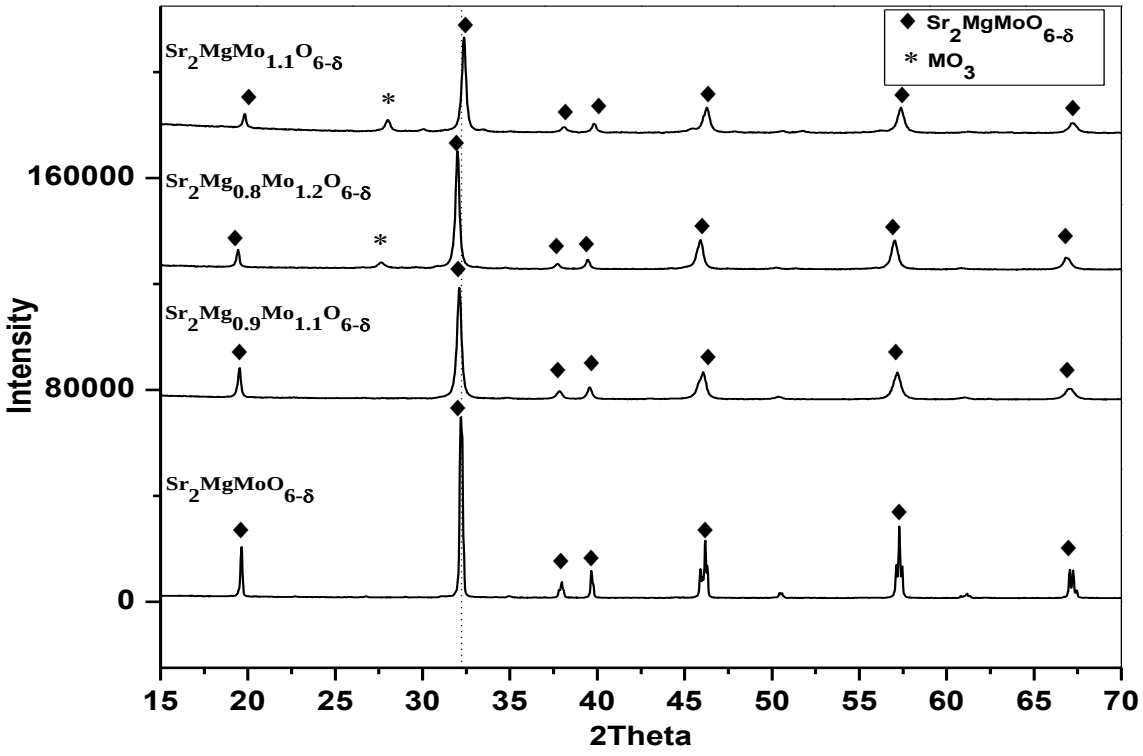

Figure 26. XRD pattern of Sr2MgMoO6-δ, Sr2Mg1-xMo1+xO6-δ (x = 0.1 and 0.2) and Sr2MgMo1.1O6-δ prepared via solid state synthesis

Figure 27 shows the shift in the high intensity peak of $Sr_2Mg_{1-x}Mo_{1+x}O_{6-\delta}$ (x = 0.1 and 0.2) and $Sr_2MgMo_{1.1}O_{6-\delta}$ from stoichiometric SMM. It can be seen that for $Sr_2Mg_{1-x}Mo_{1+x}O_{6-\delta}$ (x = 0.1 and 0.2), while maintaining the BB'-site stoichiometry, the peak shifts towards the left indicating a reduction in the lattice parameters thereby increasing the bond strength of the elements in the perovskite structure. Whereas for $Sr_2MgMo_{1.1}O_{6-\delta}$, the peak shifts towards the right, as a result of expansion in the unit cell, caused by additional strain in the lattice. From the XRD analysis alone, one can speculate about the redox behavior of the material under.

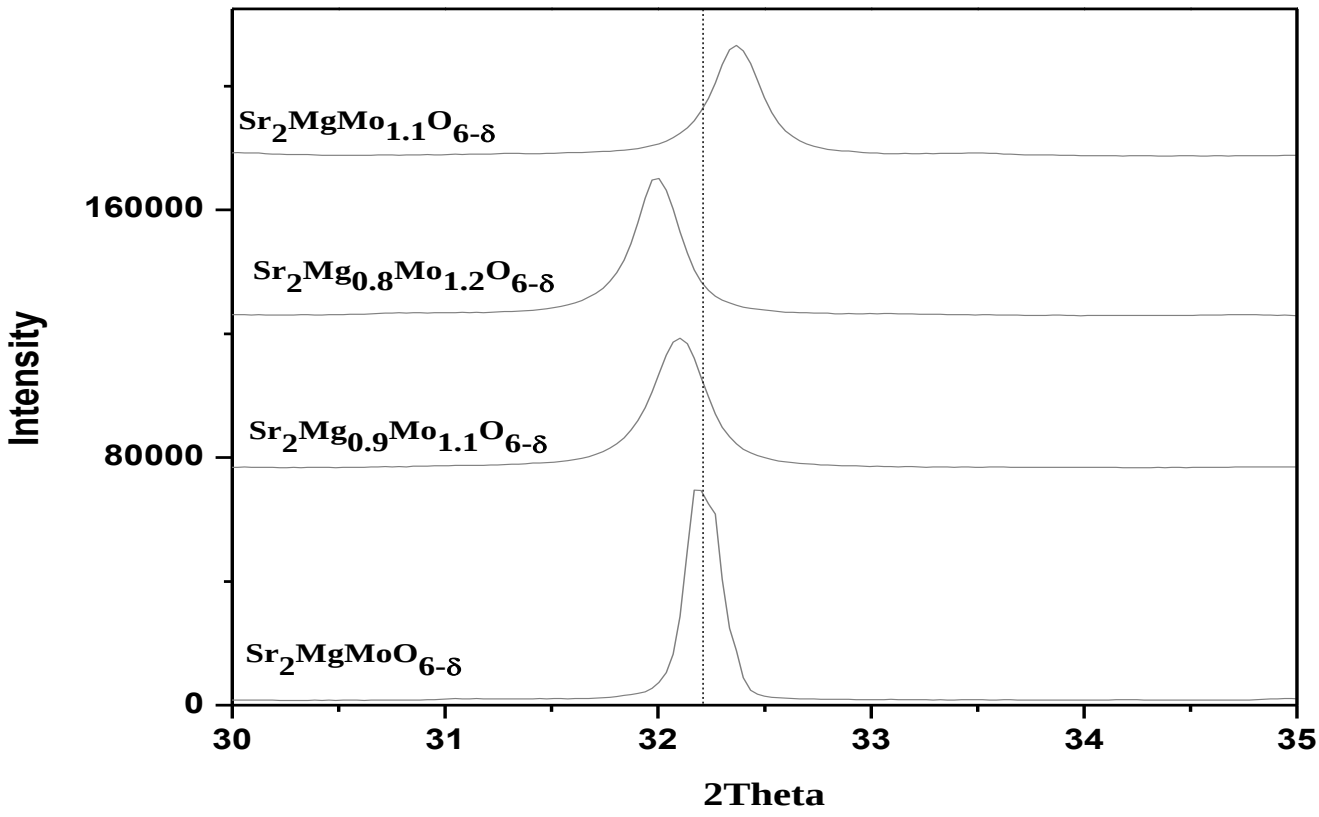

Figure 27. Shift of high intensity peak w.r.t $Sr_2MgMoO_{6-\delta}$ in $Sr_2Mg_{1-x}Mo_{1+x}O_{6-\delta}$ (x = 0.1 and 0.2) and $Sr_2MgMo_{1.1}O_{6-\delta}$ prepared via solid state synthesis

5.3.2 Thermomechanical characterization of SMM samples

The bar sample of 25 mm x 2.5 mm x 2.5 mm as shown in Chapter 2, Figure 9, was cut from the sintered pellet, as explained in the experimental section. Figure 28 shows, the dilatometry of $Sr_2MgMoO_{6-\delta}$ in air as a baseline measurement.

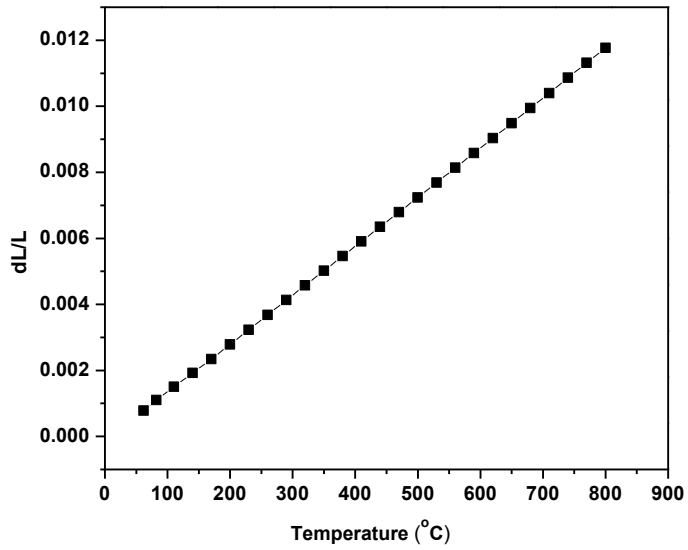

Figure 28. Dilatometry of $Sr_2MgMoO_{6-\delta}$ in air from 25-800°C

It was found that the coefficient of thermal expansion (CTE) is 15.11×10^{-6} K^{-1}. Compared to $Sr_2MgMoO_{6-\delta}$, NiO has a CTE of 14.9×10^{-6} K^{-1} and the NiO/YSZ composite has a CTE of 12.3×10^{-6} K^{-1} [96]. Hence, if SMM is found to be a good anode material, the CTE could be matched closer to YSZ by compositing SMM with the GDC electrolyte (13.23×10^{-6} K^{-1}) [97] which has a CTE close to YSZ. Also, GDC may be required within the anode composition in order to compensate for the limited ionic conduction of the SMM composition.

To assess the thermal redox stability, the samples were subjected to redox dilatometry between 25 – 800°C as per the protocol shown in Figure 10. Segment 1-2 is the ramping stage to 800°C at 3°C/min in air, Segment 2-3 is the isothermal hold for 2 h at 800°C before the redox cycling, Segment 3-7 is isothermal hold for 20 h at 800°C with automated atmospheric change from oxidizing (compressed air) to reducing (forming gas, 5%H_2-95%N_2), with each cycle performed for 10 h and Segment 7-8 is ramping down the

temperature to RT at 3°C/min in air. Figure 29, is the redox dilatometry of the $Sr_2MgMoO_{6-\delta}$ composition.

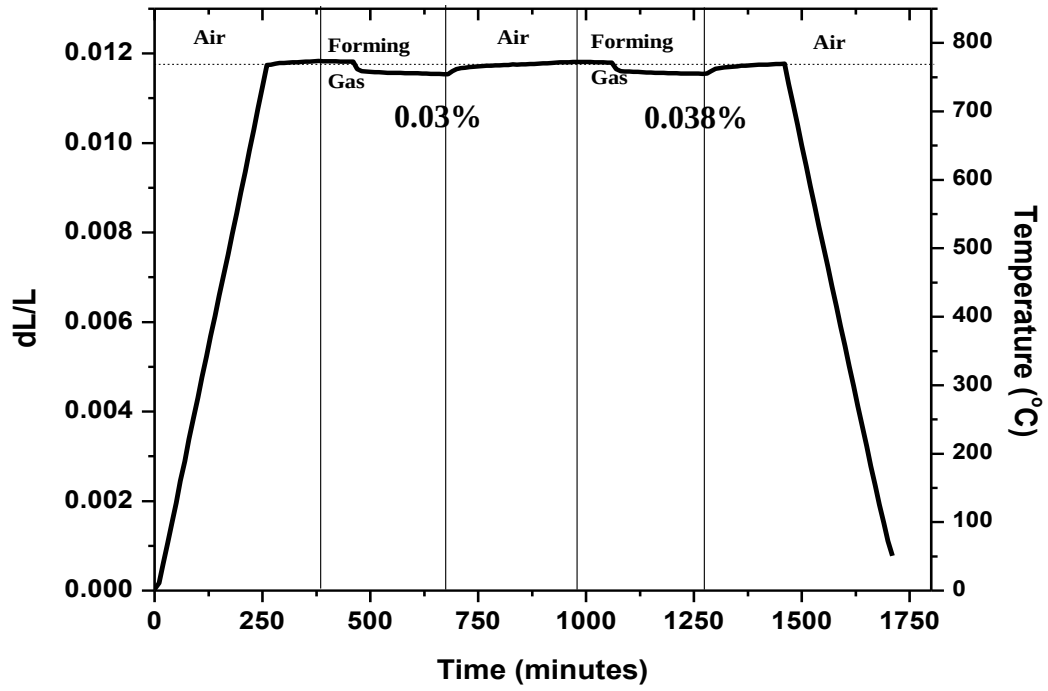

Figure 29. Redox dilatometry of $Sr_2MgMoO_{6-\delta}$

As seen in Figure 29, the stoichiometric $Sr_2MgMoO_{6-\delta}$ experiences a 0.03% volumetric reduction in the first redox cycle and 0.038% volumetric reduction in the consecutive redox cycle. The reason for the volumetric reduction is due to the oxygen vacancies formed during the reduction and also Mo vacancies formed by the loss of Mo due to its high vapor pressure. It was found that the sintered sample from which the bar samples were made for the dilatometry, had a weight reduction of 15.6%. Some percentage of this loss can be attributed to the loss of Mo, making the as-synthesized composition Mo deficient.

A volumetric reduction of the sample is observed in the reduction cycle of the dilatometry. Nevertheless, the volumetric reduction is reversible in nature as seen in Figure 29. The B/B'-site ratio was varied in the stoichiometric $Sr_2MgMoO_{6-\delta}$, while still maintaining the double B-site stoichiometry as $Sr_2Mg_{1-x}Mo_{1+x}O_{6-\delta}$ (x = 0.1 and 0.2) (refer to Figure 26). This indeed was an effort to increase the Mo content, as the formation of Mo^{5+} enhances

the electronic conductivity. The composition with B' site hyper stoichiometry ($Sr_2MgMo_{1.1}O_{6-\delta}$) was also prepared to analyze the effect of excess Mo on the thermal and electrical redox stability. It was observed that $Sr_2Mg_{0.9}Mo_{1.1}O_{6-\delta}$ had a weight reduction of 2.94% after sintering, whereas $Sr_2Mg_{0.8}Mo_{1.2}O_{6-\delta}$ and $Sr_2MgMo_{1.1}O_{6-\delta}$ lost about 2.6% of weight after sintering. This is a huge improvement in weight loss from 15.6% to just around 3%, indicating less Mo deficiency upon varying B/B'-site ratio. Figure 30 is the redox dilatometry plot of $Sr_2Mg_{0.9}Mo_{1.1}O_{6-\delta}$, $Sr_2Mg_{0.8}Mo_{1.2}O_{6-\delta}$ and $Sr_2MgMo_{1.1}O_{6-\delta}$. Redox behavior of $Sr_2Mg_{0.9}Mo_{1.1}O_{6-\delta}$, is as same as $Sr_2MgMoO_{6-\delta}$, but the percentage change in volume was reduced to 0.017% from 0.03%. This is due to the minimization of Mo deficient sites resulting from the change in the Mg/Mo ratio. $Sr_2Mg_{0.8}Mo_{1.2}O_{6-\delta}$ and $Sr_2MgMo_{1.1}O_{6-\delta}$ (data points are overlapped in Figure 30) exhibit a similar thermal redox behavior, but with every cycle the material expands in air, thus failing to achieve redox stability. This may be due to the MoO_3 secondary phase (refer to Figure 26) in these compositions, which affects the thermal redox stability. Table 5 summarizes the change in CTE of the compositions with different Mg/Mo ratio. The CTE of the material drops as the Mo content increases compared to $Sr_2MgMoO_{6-\delta}$ while keeping the B-site stoichiometry. This is due to the reduction in the volume of the unit cell as confirmed by the XRD, (refer to Figure 27) resulting in an increase in inter-material bond strength. On the other hand, the CTE of non-stoichiometric B–site compositions increases to 15.61×10^{-6} K^{-1} due to the expansion in the unit cell (refer to Figure 30). Thus there is a substantial effect on the thermal behavior, when the Mg/Mo ratio is varied. The next section addresses the effect of changing the Mg/Mo ratio on the electrical conductivity.

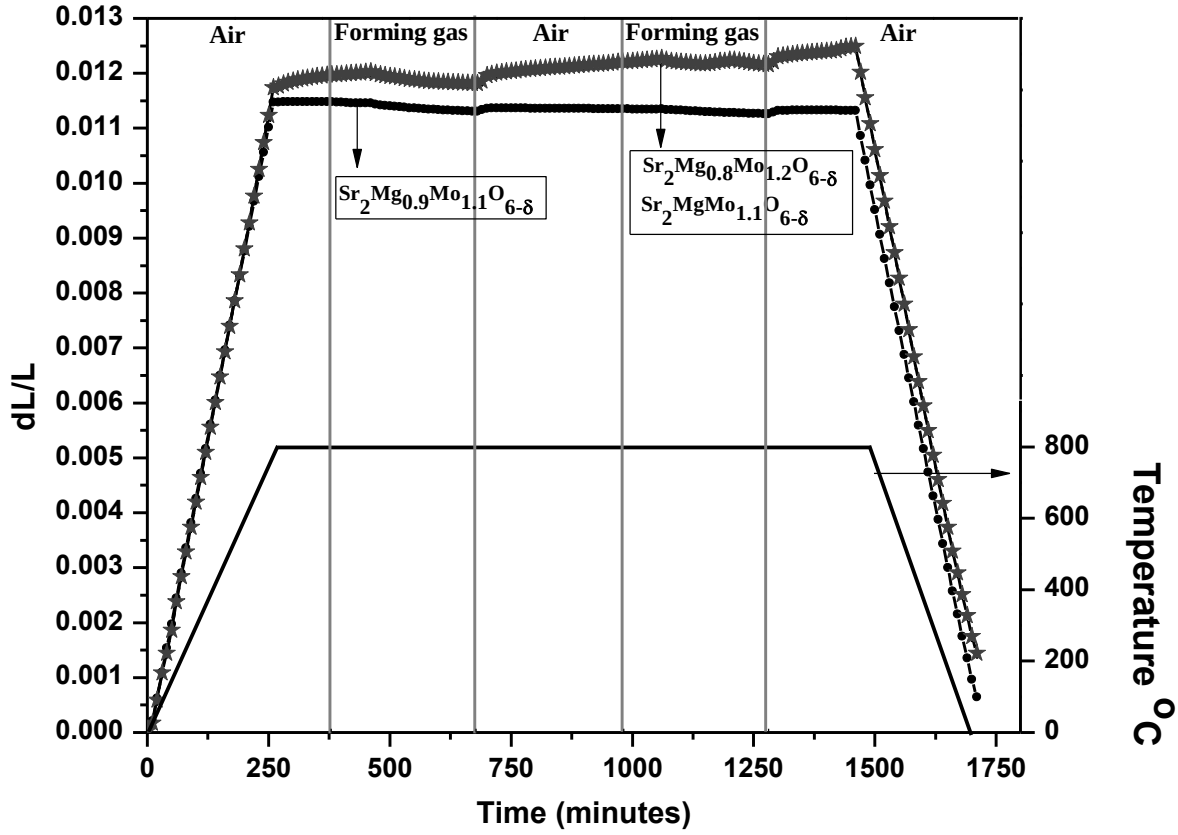

Figure 30. Redox dilatometry $Sr_2Mg_{0.9}Mo_{1.1}O_{6-\delta}$, $Sr_2Mg_{0.8}Mo_{1.2}O_{6-\delta}$ and $Sr_2MgMo_{1.1}O_{6-\delta}$ between 25-800°C

Table 5. The change in CTE with different Mg/Mo ratio

Composition	Mg/Mo (moles)	CTE x 10^{-6} K^{-1}
$Sr_2MgMoO_{6-\delta}$	1/1	15.11
$Sr_2Mg_{0.9}Mo_{1.1}O_{6-\delta}$	0.9/1.1	14.40
$Sr_2Mg_{0.8}Mo_{1.2}O_{6-\delta}$	0.8/1.2	14.50
$Sr_2MgMo_{1.1}O_{6-\delta}$	1/1.1	15.61

5.3.3 Electrical characterization

Table 6 summarizes the electrical behavior of the materials for three redox cycles at 800°C. The stoichiometric $Sr_2MgMoO_{6-\delta}$ recorded a maximum conductivity of 50 S/cm in the first reduction cycle, and with consecutive reduction cycles, the conductivity dropped by more than half of the first reduction cycle. From the redox dilatometry, a permanent deformation of about 0.008% was measured after the first redox cycle. Though it is not substantial in terms of absolute value, it can introduce micro cracks in the material as seen in Figure 31, thus disrupting the electron conducting channel with each redox cycle. The conductivity of $Sr_2MgMoO_{6-\delta}$ in air was a constant of 0.01 S/cm owing to the fact that Mo^{6+} does not favor electronic conductivity and this value relates to the ionic conductivity of the material, which can be compared to that of 8YSZ at 800°C [98].

Table 6. Effect of Mg/Mo ratio on redox electrical behavior of the materials at 800°C

Composition	1st oxidation cycle (S/cm)	1st reduction cycle (S/cm)	2nd oxidation cycle (S/cm)	2nd reduction cycle (S/cm)	3rd oxidation cycle (S/cm)	3rd reduction cycle (S/cm)
$Sr_2MgMoO_{6-\delta}$	0.01	50	0.01	28	0.01	20
$Sr_2Mg_{0.9}Mo_{1.1}O_{6-\delta}$	0.1	17	0.1	17.5	0.1	17.5
$Sr_2Mg_{0.8}Mo_{1.2}O_{6-\delta}$	30.8	42.2	27.6	38.6	-	-
$Sr_2MgMo_{1.1}O_{6-\delta}$	28.9	250	30	31	30.6	31.6

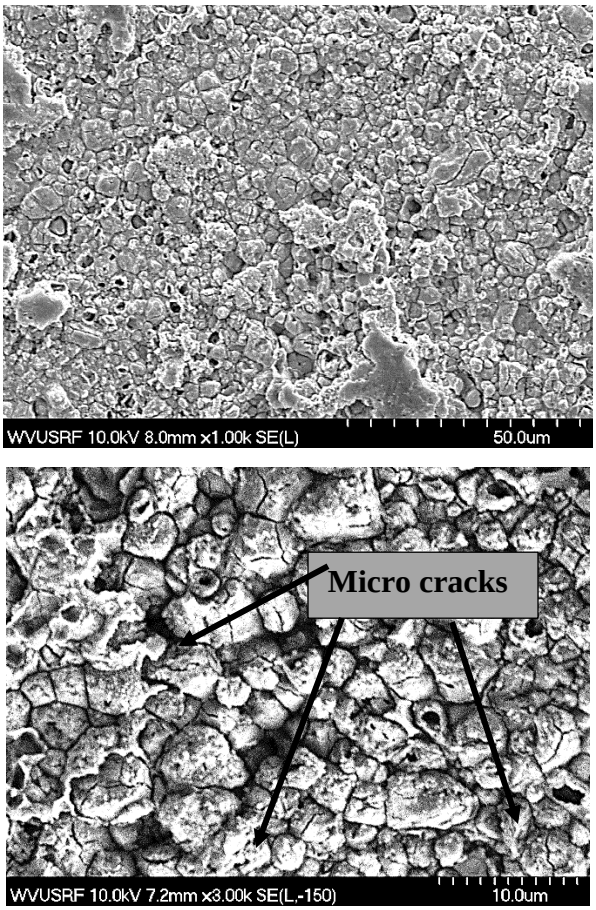

Figure 31. (Left) $Sr_2MgMoO_{6-\delta}$ surface before redox cycling. (Right) Micro cracks formed on the $Sr_2MgMoO_{6-\delta}$ surface after redox cycling

In the thermal characterization section, the effect of Mg/Mo ratio on redox thermal behavior was demonstrated and it can be extended to its electrical redox behavior as well. For the Mg/Mo ratio 0.9/1.1 a pure phase composition was obtained, but the high intensity peak shifted to the left, indicating a decrease in the unit cell volume. The resultant stronger bond strength enhanced the electrical redox stability of the material along with its thermal stability. $Sr_2Mg_{0.9}Mo_{1.1}O_{6-\delta}$ showed a consistent total electrical conductivity of 17.5 S/cm for all three reduction cycles and a meager electrical conductivity of 0.1 S/cm in the oxidizing environment. This composition exhibited total redox stability in terms of thermal and electrical properties at 800^{o}C. For the Mg/Mo ratio 0.8/1.2, the total electrical conductivity increased to 42.2 S/cm in the first cycle, which is higher than $Sr_2Mg_{0.9}Mo_{1.1}O_{6-\delta,}$ due to the excess 0.1 mole of Mo. But as noticed in redox dilatometry tests, this composition expands irreversibly at 800^{o}C with consecutive redox cycles. This

causes micro-cracking through the bulk of the material, affecting its electrical properties. Hence, in the second reducing cycle the conductivity dropped to 38.6 S/cm. The increase in oxygen vacancies due to the secondary MoO_3 phase improved the electrical conductivity in air almost 300 times compared to $Sr_2Mg_{0.9}Mo_{1.1}O_{6-\delta}$. The final composition with non-stoichiometric BB'-site, i.e. the Mg/Mo ratio 1/1.1, showed the maximum conductivity of 250 S/cm in the first reducing cycle compared to the other compositions in this study. The XRD analysis (refer Figure 27) of this composition showed a right shift of the high intensity peak with respect to the stoichiometric $Sr_2MgMoO_{6-\delta}$ high intensity peak, indicating an increase in the unit cell volume. This aspect resulted in further mechanical instability with each redox cycle. As in this case, the conductivity dropped to 31 S/cm in the consecutive cycle and maintained this conductivity value in the subsequent redox cycles. This means that the material attains a general level of redox stability after the first redox cycle. Figure 32 shows the variation of the electrical conductivity with increasing temperature in both oxidizing (Figure 32a) and reducing (Figure 32b) environments. From the following experiments, $Sr_2MgMoO_{6-\delta}$, $Sr_2Mg_{0.9}Mo_{1.1}O_{6-\delta}$ and $Sr_2MgMo_{1.1}O_{6-\delta}$ were found to be mechanically redox stable with good electrical conductivity required for the material to pass as a SOFC anode material. Further studies will be undertaken to evaluate the effective polarization resistance (R_p) of these materials by symmetrical cell testing in $5\%H_2/95\%$ and finally these materials will be put to test in a fuel cell set up to evaluate their catalytic activity as well as performance under actual cell operating conditions.

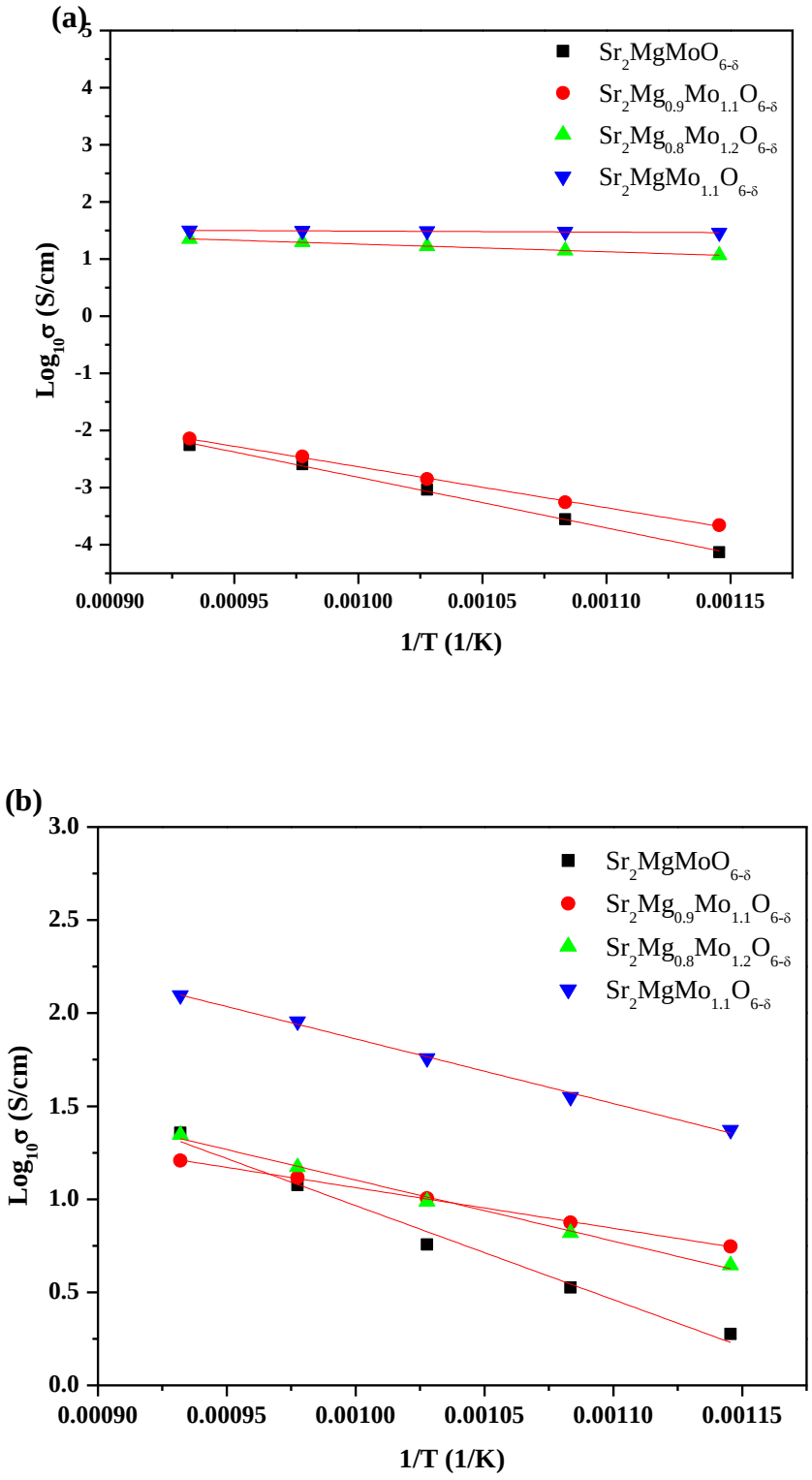

Figure 32. Electrical conductivity of $Sr_2MgMoO_{6-\delta}$, $Sr_2Mg_{1-x}Mo_{1+x}O_{6-\delta}$ (x = 0.1 and 0.2) and $Sr_2MgMo_{1.1}O_{6-\delta}$ between 25-800ºC (a) In oxidizing atmosphere, (b) In reducing atmosphere

5.4 Conclusion

$Sr_2MgMoO_{6-\delta}$ has been proposed as a good anode material for SOFC applications due to its resistance to coking, sulphur poisoning and potential redox stability. From this work, it was found that stoichiometric $Sr_2MgMoO_{6-\delta}$ showed ~0.008% permanent deformation (strain). The volumetric reduction of $Sr_2MgMoO_{6-\delta}$ in a reducing atmosphere caused micro-cracking as a result of the deficient B'-site which occurs upon sintering. It was found that the material loses 15.6% of its total weight after sintering, and some percentage of this weight can be attributed to Mo loss as it is the only species with high vapor pressure in the system. To address this issue, the Mg/Mo ratio was varied keeping the BB'-site stoichiometric while the Mo content was increased as $Sr_2Mg_{1-x}Mo_{1+x}O_{6-\delta}$ (x = 0.1 and 0.2). From the redox thermal and electrical analysis, it can be concluded that $Sr_2Mg_{0.9}Mo_{1.1}O_{6-\delta}$ is redox stable. $Sr_2Mg_{0.8}Mo_{1.2}O_{6-\delta}$ showed continuous volumetric expansion upon cycling due to the inclusion of the MoO_3 secondary phase. Though $Sr_2Mg_{0.8}Mo_{1.2}O_{6-\delta}$ showed higher electrical conductivity than $Sr_2Mg_{0.9}Mo_{1.1}O_{6-\delta}$ due to higher Mo content, the electrical conductivity dropped by a small amount. The excess Mo in the non-stoichiometric BB'-site composition ($Sr_2MgMo_{1.1}O_{6-\delta}$) showed similar thermal behavior as $Sr_2Mg_{0.8}Mo_{1.2}O_{6-\delta}$, but recorded the highest electrical conductivity of 250 S/cm (first reduction cycle) compared to the other compositions. With subsequent redox cycling, the electrical conductivity dropped substantially, but achieved stability on further cycling. In the future, XPS studies should be carried out to understand the oxidation state of Mo in these compositions and also to evaluate the oxygen vacancy concentration. These results will be related to the anode polarization during fuel cell testing over prolonged loading.

Chapter 6. Summary

6.1 Introduction

This chapter is intended to summarize the outcome of the research study carried out in this MS by research course. In addition suggestions on possible future work on some of the above chapters which can be useful for augmenting this research have been reported in this chapter.

6.2 Developing High Temperature Redox Dilatometry Testing Protocol

A testing protocol has been developed to analyze the thermal redox behavior of newly developed anode materials for SOFC application. This is in an attempt to speed through the material development process, as development of new anode materials is time consuming, labor intensive and expensive. A simple push rod type dilatometer has been used in the characterization of high-temperature redox behavior of materials by automating the timely introduction of oxidizing and reducing atmospheres in order to simulate a cell stack leak. By using the present test protocol, data like coefficient of thermal expansion (CTE), volumetric change in the cell lattice, redox behavior (volumetric expansion or volumetric reduction) and number of redox cycles before material failure can be obtained. The testing protocol has been calibrated with commonly used SOFC materials like YSZ (8 mol% yttria doped), GDC (20 mol% Gd doped), $La_{0.35}Sr_{0.65}TiO_3$ (LST) and also with LST/GDC (50/50 vol%) composite. All the materials developed in this research work were analyzed using this testing protocol to assess eligibility as a suitable anode material.

6.3 Effect of W and Mo Doping on the Redox Properties of $CeNbO_{4+\delta}$

In an attempt to convert $CeNbO_{4+\delta}$ into a mixed ionic and n-type conductor, the pentavalent Nb-site was doped with hexavalent tungsten and molybdenum and its effect on the thermomechanical redox stability and total electrical conductivity was studied with respect to the parent $CeNbO_{4+\delta}$. XRD analysis at room temperature revealed biphasic Monoclinic I2/a and Tetragonal $I4_1/a$ crystal systems. The formation of a scheelite phase was observed at 10 and 20 mol% doped W and 10 mol% dopes Mo. Hence $CeNbO_{4+\delta}$, $CeW_{0.1}Nb_{0.9}O_4$, $CeW_{0.2}Nb_{0.8}O_4$ and $CeMo_{0.1}Nb_{0.9}O_4$ were the compositions under investigation. XPS analysis identified the atomic concentration (at %) ratio of Ce^{3+} and Ce^{4+} in the parent

material and how this ratio varied with B-site doping. It was found that, in $CeNbO_{4+\delta}$, Ce^{3+} to Ce^{4+} ratio is 14.5, whereas $CeNb_{0.9}Mo_{0.1}O_4$ and $CeNb_{0.8}W_{0.2}O_4$ this ratio is 4.55 and 3.17 respectively. The thermomechanical redox stability upon doping was confirmed by dilatometry and TGA, where the materials exhibited reversible volumetric change upon redox cycling. A four-point DC probe of electrical conductivity confirmed the redox stable conductivity properties of the B-site doped material as compared to the parent $CeNbO_{4+\delta}$. Though it was possible to improve the mechanical redox stability of this material by adopting these doping strategies, their electrical conductivity was not as high as a typical anode material. But it can be noticed that $CeNbO_{4+\delta}$ has a conductivity of 0.13 S/cm in air at 650^{o}C, which is an order of magnitude higher than YSZ at 800^{o}C. Hence it has a potential to be used as a low temperature SOFC electrolyte.

6.4 Thermo-Mechanical Redox Stability Analysis of Nb_2TiO_7 and $Nb_{1.33}Ti_{0.67}O_4$ for SOFC Application

Nb_2TiO_7 and $Nb_{1.33}Ti_{0.67}O_4$ have been reported as potential anode materials for Solid Oxide Fuel Cells (SOFCs) based on their stable reversible phase transformation and high electronic conductivity. XRD analysis confirmed the phase purity. From high-temperature redox dilatometry the linear expansion or contraction of Nb_2TiO_7 and $Nb_{1.33}Ti_{0.67}O_4$ synthesized through a solid-state route was monitored. It was found that Nb_2TiO_7 contracts linearly up to 0.006% in a reducing atmosphere and this contraction is reversible in nature whereas $Nb_{1.33}Ti_{0.67}O_4$ expands linearly up to 1.9% in an oxidizing atmosphere which is irreversible in nature at 800^{o}C. Also the electrical conductivity of the materials was analyzed in redox atmospheres. At 800^{o}C, Nb_2TiO_7 has an electrical conductivity of 1.35 S/cm in forming gas (5%H_2/95%N_2) which increases to 85 S/cm upon the reduction of Nb_2TiO_7 to $Nb_{1.33}Ti_{0.67}O_4$. Due to the extrinsic and intrinsic complications of the material properties, single phase Nb_2TiO_7 as a starting composition is not an ideal anode candidate for SOFC applications. But compositing Nb_2TiO_7 with materials like $Gd_{0.1}Ce_{0.9}O_2$ can enhance its conductivity and catalytic properties for SOFC application. If $Nb_{1.33}Ti_{0.67}O_4$ is used as the starting anode composition, adopting different B site doping strategies to increase the unit cell volume to match the unit cell volume of Nb_2TiO_7 can be a feasible approach to use $Nb_{1.33}Ti_{0.67}O_4$ as an SOFC anode. Also the range of conductivity

demonstrated by Nb_2TiO_7 in high pO_2 and low pO_2 atmosphere makes it suitable as a gas sensor that senses the change in resistivity of the material due to gas adsorption.

6.5 Effect of Mg/Mo Ratio in a Stoichiometric Sr2MgMoO6-δ (SMM) Redox-Stable Anode

Stoichiometric SMM has a conductivity of ~50 S/cm in a reducing atmosphere but with consecutive redox cycling, the conductivity decreases. Effort has been made to understand the reason for the drop in electrical conductivity with increasing redox cycling. It has been found that the Mo concentration may change with time at 800^oC, accounting for the drop in conductivity. This work investigated the electrical performance of the SMM composition as a function of Mg/Mo ratio and level of excess Mo. In addition, the work investigated the thermal and electrical stability as a function of operation and thermal cycling. It was found that at a Mg/Mo ratio of 0.9/1.1, the material achieved both thermal and electrical redox stability. From redox dilatometry, it was found that $Sr_2Mg_{0.9}Mo_{1.1}O_{6-\delta}$ experienced a reversible volumetric reduction of 0.017% and had a reversible electrical conductivity of 17.5 S/cm in a reducing atmosphere. From the following experiments, $Sr_2MgMoO_{6-\delta}$, $Sr_2Mg_{0.9}Mo_{1.1}O_{6-\delta}$ and $Sr_2MgMo_{1.1}O_{6-\delta}$ were found to be mechanically redox stable with good electrical conductivity required for the material to pass as a SOFC anode material. Further studies will be undertaken to evaluate the effective polarization resistance (R_p) of these materials by symmetrical cell testing in 5%H_2/95% and finally these materials will be put to test in a fuel cell to evaluate their catalytic activity as well as performance under actual cell operating conditions.

References

[1] Q. M. Nguyen, J. Am. Ceram. Soc., (1999) 76(3), pp 563–588.

[2] J. Galdo, United States Department of Energy Headquarters, Bologna Conference on Fuel Cells. Italy. May 31–June 01 (2001)

[3] S. C. Singhal, Encyclopedia of Applied Electrochemistry, 2014, Springer, pp 2010

[4] M. Hans-Heinrich, S.C. Singhal, K. Kendall, "High temperature solid oxide fuel cells: fundamentals, design and applications" Elsevier, Oxford, UK, (2010), pp 23–25

[5] W. Nernst, "Material for electric-lamp glowers", US Patent No. 685,730 (1901)

[6] C. Wagner, Naturwissenschaften, (1943) 31, pp 265–268

[7] E. Bauer, H. Preis, Z Elektrochem, (1937) 43, pp 727–732

[8] J. Weissbart, R. Ruka, Rev Sci Instrum, (1961) 32, pp 593–595

[9] S. V. Karpachov, S. F. Palguyev, W. N. Chebotin, A. D. Neuimin, A. T. Filyayev, Tr. Inst. Elektrokhim. Akad.Nauk SSSR, Ural Filial, 1 (1960)

[10] J. Weissbart, R. Ruka, J Electrochem Soc, (1962) 109, pp 723–726

[11] H. Binder, A. Ko¨hling, H. Krupp, K. Richter, G. Sandstede , Electrochim Acta, (1963) 8, pp 781–793

[12] J. Besson, C. Deportes, M. Kleitz, editions Technip, Paris, (1965), pp 87–102

[13] K. R. Williams, J. G. Smith, Great Britain patent No. 1,049, 428, filed August 15, 1963

[14] T. Takahashi, J Electrochem Soc, (1966) 34, pp 60–69

[15] H. S. Spacil, US Patent No. 3,503,809, filed October 30,1964

[16] C. S. Tedmon, H. S. Spacil, S. P. Mitoff, J Electrochem Soc (1969) 116, pp 1170–1175

[17] D. B. Meadowcroft, Brit J Appl Phys, (1969) 2, pp 1225–1233

[18] W. Fischer, H. Kleinschmager, F. J. Rohr, R. Steiner, H. H. Eysel, Chem Ing Tech, (1972) 44, pp 726–732

[19] U. B. Pal, S. C. Singhal, J Electrochem Soc (1990) 137, pp 2937–2941

[20] S. R. Bharadwaj, S. Varma, B. N. Wani, Funct Mater (2012), pp 639–674

[21] B. C. H. Steele, A. Heinzel, Nature, (2001) 414, pp 345–52

[22] S.C. Singhal, Solid State Ionics (2000) 135, pp 305–313

[23] A.Boudghene Stambouli, E. Traversa, Renewable and Sustainable Energy Reviews, (2002) 6, pp 433-455

[24] X. Chen, N. J. Wu, Z. H. Zhang, A. Ignatiev, Thin Solid Films (1999) 350(1-2), pp 130–137

[25] M. Cassidy, G. Lindsay, K. Kendall, J Power Sour (1996) 61, pp 189–192

[26] N. M. Sammes, B. R. Roy, Encycl Electrochem Power Sources, (2009), pp 25–33.

[27] B. P. McCarthy, L. R. Pederson, Y. S. Chou, X. D. Zhou, W. A. Surdoval, J Power Sources (2008) 180, pp 294–300

[28] P. Khandale, R. P. Lajurkar, S. S. Bhoga, Int J Hydrog Energy (2014) 39, pp 19039–19050

[29] C. Jeong C, J. H. Lee, M. Park, J. Hong, H. Kim, J Power Sources (2015) 297, pp 370–378

[30] A. C. Fouquet, A. Müller, E. Weber, Ivers-Tiffée, Proc.5th European SOFC Forum Lucerne,Switzerland, (2002), pp 467

[31] D. Sarantaridis, J. Power Sources (2008) 180, pp 704-710

[32] M. Suzuki, H. Sasaki, S. Otoshi, A. Kajimura and M. Ippommatsu, Solid State Ionics, (1993) 62, pp 125

[33] S. P. Jiang and S. H. Chan, Journal of Materials, 39, 4405 (2004).

[34] C. Xu, J. W. Zondlo, M. Gong and X. Liu, Journal of Power Sources, 196(1), 116 (2011).

[35] M. Pihlatiea, A. Kaisera and M. Mogensena, Journal of the European Ceramic Society, (2009) 29(9), pp 1657 .

[36] O. A. Marina, N. L. Canfield and J. W. Stevenson, Solid State Ionics, (2002) 149, pp 21

[37] H. Hayashi, M. Kanoh, C. J. Quan and H. Tagawa, Solid State Ionics, (2000) 132, pp 227

[38] I. Yasuda, M. Hishinuma, Electrochemistry, (2000) 68, pp 526

[39] G. Mogensen and M. Mogensen, Thermochlm Acta, (1993) 214, pp 47

[40] Q. M. Nguyen, Journal of American Ceramic Society, (1993), 76, pp 563–588

[41] O. Yamamoto, Y. Takeda, R. Kanno, M. Noda,Solid State Ionics, (1987) 22, pp 241

[42] Data from The International Fuel Cells, A United Technology Company, Fuel Cells Review, (2000)

[43] H. Yokokawa, N. Sakai, T. Kawada, M. Dokiya, Solid State Ionics, (1992) 52, pp 43–56

[44] J. Canales-Vázquez, S. W. Tao, J. T. S. Irvine, Solid State Ionics, (2003) 159, pp 159–165

[45] H. Möbius, Journal of Solid State Electrochemistry, (1997) 1, pp 2

[46] S. J. Skinner, Solid State Ionics, (2002) 154, pp 325–329

[47] S. J. Skinner, Y. Kang, Solid State Science, (2003) 5, pp 1475–1479.

[48] J. G. Thompson, A. D. Rae, N. Bliznyuk, R. L. Withers, Journal of Solid State Chemistry, (1999) 144, pp 240–246

[49] J. G. Thompson, R. L. Withers, F. J. Brink, Journal of Solid State Chemistry, (1999) 143, pp 122–131

[50] R.J. Packer, J. Barlow, A. Cott, S.J. Skinner, Solid State Ionics (2008) 179, pp 1094–1100

[51] E. Çiftyürek, K. Sabolsky, E. M. Sabolsky, Sensors and Actuators B: Chemical, (2016) 237, pp 262-274

[52] S. Seal, T. Barr, Experimental Methods in the Physical Sciences, edited by H. Singh Nalwa Academic, New York, Chapter 2 (2001), pp 111–190

[53] W. Chen, C.S. Chen, L. Winnubst, Solid State Ionics, (2011) 196,pp 30–33

[54] Q. Zeng, Y.B. Zuo, C.G. Fan, C.S. Chen, Journal of Membrane Science, (2009) 335, pp 140–144

[55] J.C. Dupin, G. Danielle, V. Philippe, L. Alain, Physical Chemistry Chemical Physics, (2000) 2, pp 1319–1324

[56] J.C. Wang, D.Y. Jian, Y.R. Ye, L.C. Chang, C.S. Lai, Journal of Physics D: Applied Physics (2013) 46

[57] X. Zhang, J. Qin, Y. Xue, Y. Pengfei, B. Zhang, B. Wang, L. Wang, R. Liu,Scientific Reports (2014) 4

[58] S.K. Pandey, S.K. Pandey, U.P. Deshpande, V. Awasthi, K. Ashish, G. Mukul, M. Shaibal, Semiconductor Science and Technology, (2013) 25

[59] E. Beche, P. Charvin, D. Perarnau, S. Abanades, G. Flamant, Surface and Interface Analysis, (2008) 40, pp 264–267

[60] V.C. Minarchick, P. A. Stapleton, D. W. Porter, Cardiovascular Toxicology, (2013) 13, pp 323

[61] M.V. Rama Rao, T. Shripathi, Journal of Electron Spectroscopy and Related Phenomena, (1997) 87, pp 121

[62] G. Liu, J.A. Rodriguez, J. Hrbek, J. Dvorak, Journal of Physical Chemistry B, (2001) 105, pp 7726

[63] P. Burroughs, A. Hammett, A.F. Orchard, G. Thornton, Journal of Chemical Society, Dalton Transactions, (1976), pp 686

[64] E.J. Preisler, O.J. Marsh, R.A. Beach, T.C. McGill, Journal of Vacuum Scienceand Technology B, (2001) 19, pp 1611

[65] J. Geyer-Lippmann, A. Simon, F. Z. Stollmaier, Zeitschrift für anorganische und allgemeine Chemie, (1984) 516, pp 55

[66] T. A. Sasaki, Y. Baba, Physical Review B, (1985) 31, pp 791

[67] G. E. McGuire, G. K. Schweitzer, T. A. Carlson, Inorganic Chemistry, (1973) 12, pp 2451

[68] R. J. Packer, S. J. Skinner, A. A. Yaremchenko, E. V. Tsipis, V. V. Kharton, M. V. Patrakeevc, Yu. A. Bakhteevac, Journal of Materials Chemistry, (2006) 16, pp 3503-3511

[69] S.J. Skinner R.J. Packer, R.D. Bayliss, B. Illy, C. Prestipino, M.P. Ryan, Solid State Ionics, (2011) 192, pp 659-663

[70] V.V. Kharton, F.M.B. Marques, A. Atkinson, Solid State Ionics, (2004) 174, pp 135–149

[71] Hideko Hayashi, Mariko Kanoh, Chang Ji Quan, Hideaki Inaba, Shaorong Wang Masayuki Dokiya, Hiroaki Tagawa, Solid State Ionics, (2000) 132, pp 227–233

[72] G. Mogensen, M. Mogensenb, Thermochzmzca Acta, (1993) 214, pp 47-50

[73] R.J. Packer, E.V. Tsipis, C.N. Munnings, V.V. Kharton, S.J. Skinner, J.R. Frade, Solid State Ionics, (2006) 177, pp 2059–2064

[74] E.V. Tsipis, V.V. Kharton, N.P. Vyshatko, A.L. Shaula, J.R. Frade, J. Solid State Chem, (2003) 176, pp 47

[75] R.N. Basu, G. Blass, H.P. Buchkremer, D. Stöver, F. Tietz, E. Wessel, I.C. Vinke, J. Eur. Ceram. Soc, (2005) 25, pp 463-471

[76] M. Pihlatie, A. Kaiser, M. Mogensen, J. Eur. Ceram. Soc, (2009) 29, pp 1657-1664

[77] Y.H. Huang, R. I. Dass, Z.L. Xing, J. B. Goodenough,Science, (2006) 312, pp 254-257

[78] K. R. Thampi, A. J. McEvoy, J.J. Van herle, Electrochem. Soc, (1995) 142, pp 506-513

[79] Q. Ma, F. tietz, A. Leonide, E. I. Tiffee, Electrochem. Comm, (2010) 12, pp 1326-1328

[80] P.R. Slater, J. T. S. Irvine, Solid State Ionics, (1999) 120, pp 125-134

[81] P. R. Slater, J.T.S. Irvine, Proc. 3rd Euro SOFC Forum (1998), pp 417

[82] C. M. Reich, A. Kaiser, J. T. S. Irvine, Fuel Cells, (2001) 1, pp 249-255

[83] S. Li, J. Cheng, X. Zhang, Y. Wang; K. Xie, Chin. J. Chem. Phys, (2015) 28, pp 323-330

[84] A. Lashtabeg, J.T.S. lrvine, A. Feighery, Ionics, (2003) 9, pp 220-226

[85] D. M. Bastidas, S. W. Tao, J. T. S. Irvine, J. Mater. Chem, (2006) 16, pp 1603-1605

[86] A. Lashtabeg, J. C. Vazquez, J. T. S. Irvine, J. L. Bradley, Chem. Mater, (2009) 21, pp 3549-3561

[87] R. Fontaine, R. Caillat, L. Feve, M. J. Guittet, J. Electron Spectrosc. Relat. Phenom, (1977) 10, pp 349-357

[88] A. Darlinski, Halbritter, J. Surf. Interface Anal, (1987) 10, pp 223-237

[89] M. K. Bahl, J. Phys. Chem. Solids, (1975) 36, pp 485-491

[90] S. W. Tao and J. T. S. Irvine, Nat. Mater., 2, 320 2003.

[91] S. W. Tao and J. T. S. Irvine, J. Electrochem. Soc., 151, A252 2004.

[92] Y. H. Huang, R. I. Dass, J. C. Denyszyn, J. B.Goodenough, J. Electrochem. Soc., 153, A1266, (2006).

[93] Y. H. Huang, R. I. Dass, Z. L. Xing, J. B.Goodenough, Science, 312, 254, (2006).

[94] L. Troncoso, M. J. Martínez-Lope, J. A. Alonso, and M. T. Fernández-Díaz, J. Appl. Phys. 113, 023511 (2013).

[95] C. Bernuy-Lopez, M. Allix, C. A. Bridges, J. B. Claridge, and M. J. Rosseinsky, Chem. Mater. 19, 1035 (2007).

[96] M. Mori, T. Yamamoto, H. Itoh, H. Inaba and H. Tagawa, J. Electrochem. Soc., 145, 1374 (1998).

[97] H. Hayashi, M. Kanoh, C. J. Quan, H. Inaba, S. W. M. Dokiya and H. Tagawa, Solid State Ionics, 132, 227, (2000).

[98] S. Hui, J. Roller, S. Yick, X.Zhang, C. Decès-Petit, Y. Xie, R.Maric and D. Ghosh, J. Pow. Sour., 172(2), 493, (2007).